



HAL
open science

Oceanic versus continental influences over the last 7 kyrs from a mid-shelf record in the northern Bay of Biscay (NE Atlantic)

Aurélie Pénaud, Axelle Ganne, Frédérique Eynaud, Clément Lambert,
Pierre-Olivier Coste, Maiwen Herlédan, Muriel Vidal, Jérôme Goslin, Pierre
Stéphan, Guillaume Charria, et al.

► To cite this version:

Aurélie Pénaud, Axelle Ganne, Frédérique Eynaud, Clément Lambert, Pierre-Olivier Coste, et al.. Oceanic versus continental influences over the last 7 kyrs from a mid-shelf record in the northern Bay of Biscay (NE Atlantic). *Quaternary Science Reviews*, 2020, 229, pp.106135. 10.1016/j.quascirev.2019.106135 . hal-02895508

HAL Id: hal-02895508

<https://hal.science/hal-02895508>

Submitted on 21 Jul 2022

HAL is a multi-disciplinary open access archive for the deposit and dissemination of scientific research documents, whether they are published or not. The documents may come from teaching and research institutions in France or abroad, or from public or private research centers.

L'archive ouverte pluridisciplinaire **HAL**, est destinée au dépôt et à la diffusion de documents scientifiques de niveau recherche, publiés ou non, émanant des établissements d'enseignement et de recherche français ou étrangers, des laboratoires publics ou privés.



Distributed under a Creative Commons Attribution - NonCommercial 4.0 International License

1 **Oceanic versus continental influences over the last 7 kyrs from a mid-shelf**
2 **record in the northern Bay of Biscay (NE Atlantic)**

3
4 **Penaud A.^(a), Ganne A.^(a), Eynaud F.^(b), Lambert C.^(c), Coste P.O.^(a), Herlédan M.^(a),**
5 **Vidal M.^(a), Goslin J.^(d), Stéphan P.^(e), Charria G.^(f), Pailler Y.^(g), Durand M.^(h), Zumaque**
6 **J.⁽ⁱ⁾, Mojtahid M.^(h)**

7
8 *(a) Univ Brest (UBO), CNRS, UMR 6538 Laboratoire Géosciences Océan (LGO), F-*
9 *29280 Plouzané, France*

10 *(b) Univ Bordeaux, CNRS, UMR 5805 Environnements et Paléoenvironnements*
11 *Océaniques et Continentaux (EPOC), F-33405 Talence, France*

12 *(c) Univ Vannes (UBS), UMR 6538 Laboratoire Géosciences Océan (LGO), F-56000*
13 *Vannes, France*

14 *(d) Ifremer, Géosciences Marines, Centre de Bretagne. ZI Pointe du diable, CS 10070, F-*
15 *29280 Plouzané, France*

16 *(e) Univ Brest, CNRS, UMR 6554 Littoral Environnement Télédétection Géomatique*
17 *(LETG) Brest, F-29280 Plouzané, France*

18 *(f) Ifremer, Univ Brest, CNRS, IRD, UMR6523 Laboratoire d'Océanographie Physique*
19 *et Spatiale (LOPS), F-29280 Plouzané, France*

20 *(g) Inrap, UMR 8215 Trajectoires, IUEM, F-29280 Plouzané, France*

21 *(h) LPG-BIAF UMR-CNRS 6112, UNIV Angers, UNIV Nantes, CNRS, UFR Sciences, 2*
22 *bd Lavoisier, F-49045 Angers, France*

23 *(i) Geotop Université du Québec à Montréal, Montréal, Canada*

24
25 *Corresponding author. Tel.: +33-298-498-741; fax: +33-298-498-760.

26 *E-mail address:* aurelie.penaud@univ-brest.fr.

27

28 **Abstract**

29 We discuss paleoenvironments of north-western France over the last 7 kyrs in terms of: i)
30 long-term changes (relative sea-level rise and boreal summer insolation), ii) rapid climate
31 changes (millennial-scale Bond events and multi-decadal regimes of the North Atlantic
32 Oscillation: NAO) and iii) growing human impacts in watersheds. Our study focuses on the
33 CBT-CS11 core, retrieved in the northern Bay of Biscay, with new high-resolution (70 years)
34 palynological data (dinoflagellate cysts and pollen), combined with sedimentological and
35 oxygen stable isotopic records. This multiproxy approach enabled us to gain a better
36 understanding of the influence of varying Middle to Late Holocene climate regimes on
37 marine, coastal and terrestrial ecosystems as well as on human coastal societies. We
38 especially show that the slowdown of the relative sea-level rise, starting at around 5.9 ka BP,
39 led to the stabilization of tidal flats in estuarine environments. Subsequently, increasing river
40 flows to the ocean resulted in a progressive seasonal stratification of the shelf under
41 increasing winter precipitations and establishment of the modern winter thermohaline front at
42 3.3 ka BP. In addition, within the 4–2 ka BP interval, palynological and sedimentological
43 evidence suggests increasing river discharges in north-western France, in a context of a
44 weakened Atlantic subpolar gyre and recurrent negative “NAO-like” conditions. Finally, we
45 identified a major transition at around 1.2 ka BP (Early Middle-Ages) that appears to be
46 linked to a period of maximal anthropogenic landscape opening and soil erosion, implying
47 stronger primary productivity in coastal surface waters of the studied region.

48

49 *Keywords: Holocene; Vegetation dynamics; Stable isotopes; Atlantic subpolar gyre; Rapid*
50 *climate changes; Precipitation regimes; Winter horizontal thermohaline front.*

51

52

53 **1. Introduction**

54 **Paleoenvironmental studies of the Holocene (i.e., the last 11.7 kyrs) raise questions about**
55 **environmental changes under mixed natural and anthropogenic forcings.** However, in marine
56 sediment archives, it **is difficult** to discriminate signals induced by natural modes of climate
57 variability, integrating the complexity of atmosphere-ocean-biosphere-cryosphere-lithosphere
58 interactions, from those produced by anthropogenic activities and their impacts on the
59 surrounding watersheds. Studying Holocene sediment archives often requires interdisciplinary
60 **studies (e.g., combining** geology, geography, geochemistry, paleoecology, archaeology) **to**
61 unambiguously disentangle natural and human **signatures** of environmental changes recorded
62 in sediments.

63 Over the long-term decrease in summer insolation at boreal latitudes that started **around 9**
64 **kyrs ago** (Berger and Loutre, 1991), high-resolution Holocene studies mainly addressed the
65 question of millennial time scale climate shifts (abrupt cooling events in the North Atlantic:
66 Bond et al., 1997, 2001, also referred to as Rapid Climate Changes with a more global-scale
67 perspective including cool poles and dry tropics: e.g., Mayewski et al., 2004). Previous
68 **studies** suggested the existence of solar-induced cycles of 2,500 years throughout the
69 Holocene (e.g., Debret et al., 2009). Superimposed on the latter, a 1,500-year (e.g., Bond et
70 al., 1997, 2001; Debret et al., 2007, 2009; Wanner et al., 2008; Thornalley et al., 2009; Sorrel
71 et al., 2012) or 1,250-year (Mojtahid et al., 2019) mode of periodicity was identified **as having**
72 existed over the Middle to Late Holocene and attributed to internal forcings. Uncertainties
73 nonetheless subsist **concerning** the main drivers of these latter modes and their different
74 impacts according to the investigated area (e.g., Mayewski et al., 2004; Eynaud et al., 2018).

75 Another concern is the impact of human activities on landscapes (deforestation and land use
76 for cultures, pastoralism, **living areas and** access to terrestrial and/or marine resources;
77 Ruddiman et al., 2016) and, by **extension**, on near-continent sea-surface water characteristics
78 **(e.g., sediment supply or** coastal biodiversity) that **have** increased over the last thousand years
79 and more intensively for 4 **kyrs** in western France (e.g., Gaudin, 2004; David, 2014).
80 However, producing representative records of local anthropogenic influences can be
81 challenging depending upon where the sedimentary archive is retrieved. **For instance, local-**
82 **scale or regional-scale paleo-reconstructions depend on the proximal or distal position of the**
83 **sediment cores. Furthermore, the anthropogenic signal is less transmitted to offshore depths**
84 **(hemipelagic sediments) than to proximal sedimentary sinks (e.g., continental lakes, coastal**
85 **environments or estuarine bays).** Yet, as recently shown by the studies of Lambert et al.

86 (2017) and Ganne et al. (2016) on modern sediments from the Bay of Brest and Loire estuary
87 (western France), respectively, anthropogenic pollen signals (*Cerealia* around 1%) suffer
88 from an over-representation of arboreal pollen grains relative to the actual vegetation cover on
89 the watersheds. Along the **western** European margin, it is therefore critical to select archives
90 mitigating the proximity of continental sources with non-biased sedimentary records. **To that**
91 **end**, the northern **shelf** of the Bay of Biscay (around 100 m water depth), located in a
92 transitional domain, appears ideal for investigating Holocene rapid **and long-term**
93 paleoenvironmental changes with a **combined** land-sea approach (Naughton et al., 2007;
94 Mojtahid et al., 2019).

95 In this study, we investigate **the** CBT-CS11 **core**, retrieved in the northern part of the **Bay of**
96 **Biscay (BoBy; northern part** of the *Grande Vasière* mid-shelf sediment patch). Mojtahid et al.
97 (2019) recently **published their results on** benthic foraminiferal content, benthic oxygen and
98 carbon stable isotopes on **epibenthic species** *Cibicides refulgens*, grain-size analyses and XRF
99 data. **Their** stable oxygen isotope **measurements** on *C. refulgens* showed a significant shift
100 around 3.5–2.5 ka BP, **which they** interpreted as resulting from the onset of the modern winter
101 thermohaline front. Here, we present new **and complementary** high-resolution records of
102 dinoflagellate cyst data, pollen assemblages and benthic foraminiferal stable isotopic data on
103 *Ammonia falsobeccarii*. By **combining** our dataset with previously published geochemical and
104 sedimentological data from the CBT-CS11 core, and other sediment archives from the BoBy
105 and North Atlantic basin, our Holocene study aims to: i) document the hydrographical
106 changes on the BoBy shelf **together with vegetation changes** in north-western France
107 watersheds, and ii) **place** those changes in the complex paleoceanographic and paleoclimatic
108 context of the North Atlantic basin. This **approach allows** us to suggest synoptic mechanisms
109 explaining the main drivers for precipitation and flood regimes over the last 7 **kyrs** in the
110 studied region. Ultimately, our results will help the archaeological community integrate
111 climate forcings **into** the framework of settlements and withdrawals **from** ancient coastal sites
112 in the region since the Neolithic period.

113

114 **2. Environmental context of the Bay of Biscay**

115 ***2.1. The hydrographic pattern***

116 The Bay of Biscay (BoBy) is an open oceanic basin in the north-eastern Atlantic Ocean,
117 fringed by the Spanish and French coasts (Figure 1). **Today, seasonal** atmospheric dynamics
118 (Isemerand Hasse, 1985; Pingree and Le Cann, 1989) and **high** river discharges (e.g., Lazure
119 and Jégou, 1998; Lazure et al., 2008; Ferrer et al., 2009) **lead to** a complex system of coastal
120 currents where residual shelf currents mainly depend on wind driven, tidally induced and
121 density driven flows (e.g., Vincent and Kurc, 1969; Pingree and Le Cann, 1989;
122 Koutsikopoulos and Le Cann, 1996; Castaing et al., 1999).

123 More precisely, the circulation of the BoBy shelf can be schematized as follows (Charria et
124 al., 2013; Figure 1b): in winter (October to March), a SW-dominant wind regime forces a SE
125 to NW shelf current (with more intense currents from October to December) while, in
126 summer (April to September), dominant winds from the NW sector force a NW to SE shelf
127 current (with **greater** shelf currents from July to September). From mid-autumn to early spring
128 (thus including winter as a whole), intense river flows associated with sustained wind activity
129 maintain this region under the influence of the northward plumes of the Gironde and Loire
130 rivers along the coast, with relatively low salinities between the coast and the 100 m isobath,
131 at around 20–40 km from the coast. Freshwater discharges from the main rivers (Loire,
132 Gironde, Vilaine **and** Adour; annual mean flow around 4,200 m³/s) in surface layers thus
133 induce **steep** density gradients driving a poleward circulation (about 10 cm/s) modulated by
134 wind forcing (Lazure and Jégou, 1998; Lazure et al., 2008).

135 An along-slope seasonal current, occurring between the autumn and winter, is also
136 characterized by cyclonic circulation (Pingree and Le Cann, 1989) and an intensified
137 poleward surface flow (Iberian Poleward Current, IPC; Figure 1b). This warm and saline
138 current (Frouin et al., 1990; Pingree and Le Cann, 1992a,b; Solabarrieta et al., 2014) can
139 extend up to **the Armorican** upper slopes (**western France**; Le Cann and Serpette, 2009;
140 Garcia-Soto and Pingree, 2012).

141

142

143 **2.2. Precipitation, river discharges, winter thermohaline front**

144 The coastal environments of north-western Europe are connected to the main Atlantic
145 atmospheric regimes (e.g., North Atlantic Oscillation, NAO; East Atlantic pattern, EA). In
146 Brittany, these weather regimes and North Atlantic Sea Surface Temperatures (SSTs), are the
147 main mechanisms that drive the oceanic-rainfall regime, i.e., precipitation patterns and related
148 river discharges (Tréguer et al., 2014), as well as storminess (van Vliet-Lanoë et al., 2014).

149 During positive NAO modes, northern Europe **generally has** milder and wetter conditions and
150 has the opposite during negative modes (Hurrell, 1995; Hurrell et al., 2003). Present-day
151 environmental conditions in northern Europe (i.e., continental climate, as well as sea-surface
152 temperature and salinity changes) are thus strongly impacted by the NAO and associated
153 changes in seasonal precipitation and fluvial discharge regimes (Castaing et al., 1999; Charria
154 et al., 2013; Le Boyer et al., 2013; Tréguer et al., 2014). At the Holocene scale, previous
155 studies **have** discussed the possible role of the “NAO-like” pattern in westerly storm activity
156 within the north-eastern Atlantic **area** (van Vliet et al., 2014; Goslin et al., 2018, 2019; Pouzet
157 et al., 2018) as well as in sea-surface and bottom hydrological conditions in the northern
158 (Zumaque et al., 2017; Durand et al., 2018; Mojtahid et al., 2019) and southern BoBy (Garcia
159 et al., 2013; Mojtahid et al., 2013; Mary et al., 2017).

160 Modelling work suggested that, in winter, the Loire estuarine plume completely covers the
161 Armorican shelf in the BoBy (Lazure and Jégou, 1998). **Maximum** (/minimum) values of
162 river flows are greater than 1,500 m³/s during winter-early spring (<300 m³/s during summer)
163 (hydro.eaufrance.fr; Castaing and Allen, 1981). The confluence of marine and fluvial water
164 bodies (turbid plumes; Jouanneau et al., 1999; Lazure and Jégou, 1998), then induces a winter
165 thermohaline front **that** vertically separates bottom oceanic waters from surface freshwaters
166 (Castaing et al., 1999; Yelekci et al., 2017), and takes over with increasing summer
167 temperatures (Puillat et al., 2004). Consequently, a freshwater front also forms horizontally
168 along the 100 m isobaths in the BoBy (dotted line in Figure 1b), which **will hereafter be**
169 **referred to as the** “winter horizontal thermohaline front”.

170

171

172 **2.3. The “Grande Vasière” deposit**

173 The winter horizontal thermohaline front limits the offshore diffusion of continental
174 sediments, inducing the concentration of **fine** fluvial sediments within a massive mud patch
175 (225 km by 40 km long, ~100 m deep; Figure 1b) referred to as the *Grande Vasière* (GV;
176 Dubrulle et al., 2007). The GV designates the upper part of the Holocene sediment
177 accumulation that built up at a rate of 0.1 to 0.2 cm/year (Lesueur et al., 2001) from the
178 sedimentary infilling of the Tertiary substratum during the last marine transgression (Bourillet
179 et al., 2006). Today, the GV deposit represents a seasonal compromise between a winter
180 period of sediment advection fed by fluvial supply, and a period of higher sediment settling
181 under weakened remobilization through wave actions (storminess and distant swell) between
182 April and September (Dubrulle et al., 2007).

183 Sediment grain size is **spatially** heterogeneous over the GV, with finer sediments brought **in**
184 by fluvial turbid plumes (Jouanneau et al., 1999; Dubrulle et al., 2007). The Loire **River**
185 represents the second largest fluvial **input volume** after the Gironde ($0.5\text{--}0.6 \cdot 10^6$ t/yr) and
186 contributes about 24% of the solid sediment charge **entering** the whole BoBy (Jouanneau et
187 al., 1999). **In** the northern part of the bay, **the** Loire and Vilaine Rivers together represent 95%
188 of **the** BoBy watersheds. Up to 90% of the nutrient contribution in the northern part of the
189 Armorican shelf **comes from** the Loire **River**, Vilaine River and southern Brittany coastal
190 river discharges **making** smaller secondary contributions (Guillaud et al., 2008).

191

192 **3. Material and methods**

193 **3.1. CBT-CS11 study core and benthic foraminiferal analyses**

194 The CBT-CS11 core (47°46.429'N; 4°25.308'W; 73m depth; 3.96 m long; Figure 1) was
195 retrieved using a Calypso-Genavir corer during the CABTEX cruise (Ifremer) of the R/V
196 *Pourquoi Pas?* in June 2010 (Dussud, 2010). The lithological log of the core, CaCO₃-free
197 grain-size analyses and XRF data (1 cm resolution) are fully described in Mojtahid et al.
198 (2019), allowing the precise characterization of the deposits through time. Benthic
199 foraminiferal assemblages have also been published in Mojtahid et al. (2019), with stable
200 oxygen and carbon isotopes measured on the epibenthic species *Cibicides refulgens*, which
201 was hand-picked from the 150–250 µm fraction (113 analyses, PSO, Plouzané, Table 2). In
202 this study, we present a new isotopic dataset based on 101 analyses (~3–4 cm spacing; ~74 yr
203 resolution) of *Ammonia falsobeccarii*, also hand-picked in the 150–250 µm and analysed at
204 the PSO (Table 2). The external reproducibility (1σ) on repeated measurements of NBS19
205 international standard is ±0.04‰ and 0.09‰ for δ¹³C and δ¹⁸O, respectively.
206

207 **3.2. Palynological analyses**

208 A total of 114 samples (mean spacing of 3 cm between each) allowed us to reconstruct
209 palynological assemblages with an optimal minimum (/mean) resolution of 20 years (/70
210 years). The same palynological procedure was applied for dinocyst and pollen extraction so as
211 to allow direct comparison between terrestrial (pollen, spores and freshwater microalgae) and
212 marine (dinocysts, other marine microalgae and foraminiferal linings) microfossils on the
213 same palynological slide, thus avoiding chrono-stratigraphical issues. Palynological
214 treatments (EPOC laboratory, Bordeaux University) were conducted on the < 150 µm fraction
215 following the protocol of de Vernal et al. (1999) (Data in Brief).

216 A minimum of 300 dinocysts and 200 pollen grains were counted per level. In case of over-
217 representation of a taxon (here *Lingulodinium machaerophorum* for dinocyst assemblages),
218 counts were prolonged until at least 100 other specimens were found, keeping in mind that the
219 threshold of 100 individuals is required to identify 99% of major species (> 5%) (Fatela and
220 Taborda, 2002). Palynomorph percentages (%) and concentrations (taxa/cm³) were then
221 calculated (Table 2). Palynological taxonomical diversity was quantified by statistical
222 analyses using the “Past version 1.75b” program (Hammer et al., 2001; indexes explained in
223 Harper, 1999) (Table 2). In this study, we also established palynological ratios used for the

224 discussion of the main results (briefly detailed in Table 2) based on statistical analyses and
225 described in **Data in Brief**.
226

227 **3.3. Radiocarbon dates**

228 **By adding four more** AMS-¹⁴C dates (**three** on lamellibranches and **one** on *Turritella*
229 *communis*) to **those from** the study of Mojtahid et al. (2019), **we were able to build** a robust
230 chrono-stratigraphy based on 25 dates; six dates being excluded from the final age model
231 (Table 1, Figure 2a). All dates were calibrated (Table 1) with Calib 7.1 software, using the
232 calibration curve IntCal13 (Stuiver and Reimer, 1993; Reimer et al., 2013), considering a
233 reservoir age of -324 years to radiocarbon dates (age reservoir for western Brittany, Sein
234 Island, Mangerud et al., 2006). The age model was then established using the *Bchron* package
235 in R version 3.5.1 (Figure 2b), **allowing the** reconstruction of the last 7 **kyrs** with mean
236 sedimentation rates of 74 cm/kyr from the base of the core to 5.5 ka BP, 33 cm/kyr from 5 to
237 1.8 ka BP, and 72 cm/kyr from 1.8 ka BP to the top of the core (Figure 2a). The top of the
238 core is assumed to **have been** reworked because of chronological issues (Mojtahid et al., 2019;
239 **Figure 2a**). Also, in this study, three pollen grains of *Zea mays* were observed at 44, 47 and 54
240 cm. Around the BoBy, maize cultivation **began** in northern Spain and France in the 17th
241 century (Tenaillon and Charcosset, 2011), before **really** taking off in 1950. Thus, the rare
242 grains observed in marine cores **tend rather to be from the post-1950 period. Even though our**
243 **numerous dates could support extrapolation to the top of the core, as a precaution, only data**
244 **up to 60 cm (0.5 ka BP in age) will be discussed in this manuscript.**

245

246
247

4. Palynological results and their associated interpretation

248 The description of palynological results led us to consider three main limits (A, B and C;
249 introduced in Figure 3), as well as five palynozones (CBT 1 to CBT 5; shown in Figure 4
250 only). These boundaries/zones were established based on pollen and dinocyst observations in
251 terms of both concentrations and percentages. In the following discussion, only limits A to C
252 will be placed on Figures 5 to 10 to maintain the same scope as in the result section of this
253 manuscript. Raw data are available in [Data in Brief](#) with a full description of the multivariate
254 analyses conducted on pollen and dinocyst communities with other environmental variables.

255

4.1. Dinoflagellate cysts

a. Diversity and concentrations

257 **Thirty-nine** different dinocyst taxa were identified **in the whole core**, with a mean species
258 richness (Figure 3a) of 18 different taxa per slide. From the base of the core to limit A (296
259 cm), species richness was higher than the **dataset average**, then diversity was lower than
260 average up to limit C (110 cm) and then continuously increased towards the top of the core
261 (Figure 3a). The evolution of the diversity (Margalef index; Figure 3a) was anti-correlated
262 with the trend of *Lingulodinium machaerophorum* percentages, which were higher between
263 limits A and C, with the lowest diversity being recorded on both sides of limit B (200 cm)
264 between 217 and 163 cm (yellow band on Figure 3) when *L. machaerophorum* percentages
265 (Figure 3a) as well as concentrations and fluxes (Figure 3b) were the highest.

267 Total dinocyst concentrations (Figure 3b; as well as the **dominance index**: Figure 3a) were
268 mainly **influenced** by *L. machaerophorum* occurrences and ranged between 450 and 10,500
269 cysts/cm³, with mean values of around 3,300 cysts/cm³. Therefore, we **plotted** the
270 concentrations of *L. machaerophorum* against the concentrations of other dinocysts to
271 discriminate the respective parts occupied by this species and by the rest of the community
272 (Figure 3b). **Up to** limit A, total concentrations of the other dinocysts were higher than *L.*
273 *machaerophorum* ones. **They, then followed** a similar pattern between limits A and C, except
274 in the interval “217–163 cm”, **which was** characterized by the highest *L. machaerophorum*
275 concentrations (~4,130 cysts/cm³) and fluxes (~140 cysts/cm²/yr), while the other cysts did
276 not show any major variations. Finally, from limit C onwards, concentrations of the other
277 dinocysts were highest (~5,000 cysts/cm³ from 110 cm; Figure 3b).

278

279 b. Dinocyst assemblages and dinocyst-zones

280 Overall, dinocyst assemblages were dominated by 10 autotrophic taxa: *L. machaerophorum*,
281 *Spiniferites ramosus* (group of *S. ramosus* and *Spiniferites bulloideus*), *Operculodinium*
282 *centrocarpum*, *Spiniferites lazus*, cysts of *Pentapharsodinium dalei*, *Spiniferites elongatus*,
283 *Spiniferites mirabilis*, *Spiniferites bentorii*, *Spiniferites delicatus*, *Spiniferites membranaceus*
284 (group of *S. membranaceus* and *Spiniferites belearius*), and two heterotrophic taxa including
285 *Echinidinium* spp. and *Selenopemphix quanta* (group of *S. quanta* and *Protoperidinium*
286 *nudum*) (Figure 4a). The five dinocyst zones (labelled from CBT 1 to CBT 5; Figure 4a) were
287 related to the fluctuations of major cyst taxa percentages. First zone CBT 1 was characterized
288 by the dominance of *S. ramosus*, *O. centrocarpum*, and cysts of *P. dalei*, revealing decreasing
289 trends in parallel with the progressive rise of *L. machaerophorum* percentages (Figure 4a).
290 Second zone CBT 2 was marked by a strong increase of *L. machaerophorum* percentages
291 from around 50 up to 90% at the top of the zone (Figure 4a). *S. ramosus*, *O. centrocarpum*
292 and *S. elongatus* are still abundant and their percentages gradually decreased to the end of the
293 zone. From limit B (CBT 2-CBT 3 transition), *L. machaerophorum* percentages decrease
294 onwards. *S. lazus* increased during CBT 3, while oceanic taxa (association *O. centrocarpum* -
295 *S. elongatus*) no longer reached values as high as before the *L. machaerophorum* peak. Zone
296 CBT 4 was characterized by the highest percentages of cysts of *P. dalei* while CBT 5 was
297 marked by maximal values of *S. ramosus*, although percentages of *L. machaerophorum* were
298 still significant across both zones.

299

300 **4.2. Pollen assemblages**

301 a. Diversity and concentrations

302 A total of 70 different pollen taxa were identified in the core as a whole, with a mean species
303 richness (Figure 3c) of 18 different taxa per slide. Species richness was slightly lower than 20
304 before limit C and reached 20 to 30 taxa per slide immediately after. This increase in diversity
305 was associated with the opening of the landscape (*Quercus* drop; Figure 3c) and the
306 diversification of herbaceous plants. Mean total pollen concentrations were around 2,800
307 grains/cm³ (ranging between 500 and 16,400 grains/cm³), the highest values being
308 representative of major peaks found between limits A and B, as well as in the top 60 cm.
309 Total pollen concentrations are mainly driven by trees (especially *Quercus*). In addition to the
310 type of vegetation cover, pollen production and river transport are the main factors
311 influencing the concentration of pollen grains. Thus, seasonal synchronization between these

312 two factors likely leads to much higher pollen fluxes. A disconnection between river inputs
313 and the pollination period **should have led** to an increase of other palynomorph fluxes at the
314 expense of pollen grains. It is interesting to note that until limit B, pollen concentrations were
315 higher than dinocyst ones (Figure 3d), and after limit B, total percentages of tree pollen
316 declined in parallel with increasing fluxes of *L. machaerophorum* and lower pollen grain
317 fluxes to the **shelf**. From limit C, the major observations **were** higher pollen concentrations
318 and fluxes, as well as a diversification driven by grassland taxa.

319

320 b. Pollen assemblages and pollen-zones

321 Zone CBT 1 (Figure 4b) was characterized by the dominance of arboreal pollen, mainly
322 *Quercus* and *Corylus*, *Ulmus*, *Tilia* and *Alnus* being already present. Zone CBT 2 (Figure 4b)
323 was marked by **a slight** increase of riparian trees (especially *Alnus*), *Betula*, and *Corylus*, with
324 maximal values of *Alnus* percentages being reached at the end of the zone **concomitantly** with
325 atypically high percentages of *L. machaerophorum*. Zone CBT 2 also showed a slight
326 increase of Poaceae as well as the first discrete occurrences of cultivated taxa (i.e., *Cerealia*,
327 *Secale cereale*, *Fagopyrum* at 224–227–230cm). Zone CBT 3 (Figure 4b) was then
328 characterized by a continuous and rather high occurrence of *Fagus*, while thermophilic trees
329 *Ulmus* and *Tilia* progressively faded out. This classic subboreal signature (Morzadec-
330 Kerfourn, 1974) is the expression of the mid-Holocene freshening and increasing winter
331 precipitations induced by the general decreasing summer insolation at 65°N (Naughton et al.,
332 2007). Across Zone CBT 3 (Figure 4b), *Corylus* and *Alnus* percentages decreased, with
333 *Betula* staying stable. Zone CBT 4 (Figure 4b) was marked by the highest values of Poaceae,
334 ruderal plants and *Cerealia*, while mixed oak forest declined and *Fagus* nearly disappeared
335 from the record. *Pinus* significantly increased in zone CBT 5, potentially **indicating** the
336 appearance of pine forests in the 16th century.

337

338

339 5. Discussion

340 **5.1. Offshore-nearshore dinocyst communities and the freshwater** 341 **front in the northern Bay of Biscay**

342 a. Comparing offshore-nearshore dinocyst communities in the northern Bay of Biscay

343 Dinocyst ecology **has been** thoroughly described **through** the progressive development and
344 compilation of Atlases of modern cyst distribution (Rochon et al., 1999; Marret and
345 Zonneveld, 2003; Zonneveld et al., 2013). **Nonetheless**, there **remains** a need to better
346 understand the paleohydrological signature of this complex group along onshore-offshore
347 gradients **and in the specific case of sediments from stratified, frontal and mixed-water**
348 **regions (Marret et al., 2004)**. In order to discuss ecological changes within a marine **as**
349 **opposed to a** continental context, we compared dinocyst data from three sediment cores
350 strategically located along a marine (distal or offshore) to coastal (proximal or onshore)
351 transect across the BoBy (Figure 5): i) the full-oceanic MD95-2002 core (2,174 m water
352 depth; Zumaque et al., 2017; Figure 1b) was directly influenced by the North Atlantic
353 Circulation (Frew et al., 2000); ii) the shelf CBT-CS11 core (73 m water depth; this study;
354 Figure 1b) was under mixed oceanic and winter fluvial influences; iii) the coastal “A” core,
355 collected within the Bay of Brest, **comes from a shallow** macro-estuarine environment (8 m
356 water depth; Lambert et al., 2019; Figure 1b). By including different bathymetric ranges from
357 the same temperate latitudes, we accounted for potential changes in hydrographical and/or
358 stratification conditions that may have resulted from the Holocene relative sea level (RSL)
359 rise under variable climate and/or anthropogenic forcings. **To account for the over-**
360 **representation of *L. machaerophorum* in coastal mudflats, percentages of other cyst taxa were**
361 **represented for the A and CBT-CS11 cores without considering *L. machaerophorum* counts**
362 **in the main dinocyst sum (Figure 5).**

363

364 b. General observations

365 Along Brittany’s coasts, the understanding of the modern distribution of coastal-oceanic
366 dinocyst communities was **initiated** by **studies such as those of** Rossignol (1964, 1969), Reid
367 (1974), Morzadec-Kerfourn (1974, 1977), and Wall et al. (1977), **which have been** recently
368 complemented by Ganne et al. (2016) and Lambert et al. (2017). Previous studies showed the
369 dinocyst groups of the oceanic zone (>100–150 m water depth, outer-neritic or neritic-oceanic
370 assemblages) to be characterized by *Impagidinium aculeatum*, *O. centrocarpum*, *S. mirabilis*,

371 and *S. elongatus* (with *S. ramosus* and *S. bulloideus* in addition), with *I. aculeatum* being
372 restricted solely to full-oceanic waters. In the coastal zone (inner-neritic), the association *S.*
373 *ramosus-S. bulloideus-S. bentorii* was shown to be predominant, with *S. ramosus-S. bulloideus*
374 being more specifically characteristic of the whole Iroise Sea (Figure 1b). Finally, the
375 estuarine zone was shown to be characterized by *L. machaerophorum* until the upper part of
376 the tidal zone (Morzadec-Kerfourn, 1977), which corresponds to this species' tolerance of
377 large drops in salinity and its proliferation in brackish environments (Reid, 1975; Morzadec-
378 Kerfourn, 1977, 1992, 1997). The presence of these ecological groups is shown on Figure 5
379 by the green colour (A core) to the purple colour (MD95-2002 core) for selected major cyst
380 taxa, making it possible to reveal the main estuarine to full-oceanic taxa found in the studied
381 area. Concerning CBT-CS11 cyst data (shown in pink in Figure 5), there is some evidence for
382 stratified water conditions in a shelf environment subject to both continental and oceanic
383 influences: i) estuarine to coastal quasi-monospecific assemblages of *L. machaerophorum*, ii)
384 inner-neritic assemblages characterized by the association *S. ramosus-S. bulloideus*, iii) outer-
385 neritic assemblages characterized by the association *O. centrocarpum - S. mirabilis - S.*
386 *elongatus*, as well as iv) no full-oceanic *Impagidinium*-type observations. Offshore (MD95-
387 2002), open-ocean taxa such as *I. aculeatum* (for temperate to subtropical environments) and
388 *B. tepikiense* (for northern seasonally contrasted Atlantic environments; Rochon et al., 1999;
389 Marret et al., 2004) are dominant while they are absent at mid-shelf depth (core CBT-CS11).

390

391 *c. L. machaerophorum*, tracer for freshwater plumes under phosphate deficiency?

392 At offshore locations (core MD95-2002), *L. machaerophorum* was almost absent during the
393 Holocene (always lower or equal to 2%, except between 4.5 and 2.5 ka BP when it just
394 reached 5% in some periods; Figure 5). This is consistent with the fact that offshore surface
395 conditions are influenced by the general North Atlantic circulation, while the circulation on
396 the continental shelf is influenced by mixed fluvial/tidal currents restricted to the coast. In
397 modern sediments, this taxon formed up to 30% of total cyst assemblages by 100 m water
398 depth but barely reached 5% directly after 150 m water depth in full-oceanic Atlantic
399 associations (Andreieff et al., 1971; Williams, 1971). 90 to 96% of *Lingulodinium polyedrum*
400 resting cysts, i.e., *L. machaerophorum*, were found in surface sediments from north-western
401 France estuaries (Vilaine, Loire, and Bay of Brest; Ters et al., 1968; Morzadec-Kerfourn,
402 1976, 1977; Ganne et al., 2016; Lambert et al., 2017). A front may thus prevent the offshore
403 dispersion of *L. machaerophorum* outside the region under influence of freshwater plumes
404 (Costoya et al., 2016). This freshwater front may act as a major hydrological barrier

405 preventing the transfer of fine river-borne material to the slope and the open sea near the 100
406 m isobath (Yelekci et al., 2017). In shelf sediments (CBT-CS11), the prevalence of the
407 species over neritic to oceanic cyst taxa thus suggests coastal stratified waters are subject to
408 strong continental influence. Additionally, phosphate deficiency in aquatic systems is
409 considered a major nutritional condition required to form *L. polyedrum* resting cysts, which
410 was deduced from culture experiments dedicated to investigating the sexual reproduction of
411 this bloom-forming and widely distributed dinoflagellate (Figueroa and Bravo, 2005).

412 Interestingly, *L. machaerophorum* percentages from the Bay of Brest (core A) and South
413 Brittany shelf (core CBT-CS11) showed equivalent patterns with a clear shift at 5.9 ka BP
414 (limit A; Figure 5), most likely corresponding to a marked slowdown in the rates of the RSL
415 rise identified at a regional scale (Morzadec-Kerfourn, 1995; Goslin et al., 2015; Stéphan et
416 al., 2015; Garcia-Artola et al., 2018; Figure 2a). This inflexion of RSL rise-rates likely
417 facilitated the encroachment and development of tidal flats and subsequent saltmarshes along
418 the coasts, thus fostering the development of terrestrial sedimentation (e.g., Joly and Visset,
419 2009; Menier et al., 2010; Stéphan et al., 2019). The formation of brackish marshes along the
420 estuaries may explain the proliferation of *L. machaerophorum* cysts. Major occurrences of
421 this species were particularly seen within the 4–2 ka BP interval, both in terms of percentages
422 and concentrations (yellow band on Figure 5). Massive encystments may be attributed to
423 unfavourable conditions (e.g., drops in salinity) in a context of phosphorus deficiency. This
424 hypothesis gains weight when we consider that concentrations of other dinocyst taxa and
425 overall species richness remained low, between 4 and 2 ka BP (Figures 3b and 5).

426

427 d. Winter horizontal thermohaline front establishment

428 *O. centrocarpum* percentages reached around 40% offshore (core MD95-2002) before 3.3 ka
429 BP (limit B, Figure 5; becoming inversely correlated with increasing *S. mirabilis* percentages
430 at that time), and around 20% at mid-shelf depth (core CBT-CS11), suggesting a North
431 Atlantic Current (NAC, Figure 1a) origin of this species (Turon, 1984; Rochon et al., 1999;
432 Penaud et al., 2008). The decrease in *O. centrocarpum* at 3.3 ka BP in both cores may relate
433 to a common hydrographic cause linked to a weaker NAC. Interestingly, while the oceanic *O.*
434 *centrocarpum* pattern is similar in both shelf and hemipelagic cores, the oceanic *S. mirabilis*
435 pattern (second major species in the MD95-2002 core) was not obvious beyond limit B on the
436 shelf. CBT-CS11 was then characterized by rising percentages of *S. lazus*, followed after limit
437 C by increasing values of cysts of *P. dalei*, both taxa rarely occurring within the deep-water
438 core MD95-2002 at that time, while being found in the Central Celtic Sea at 118 m depth

439 (Marret et al., 2004). Along with the influence of the Iroise Sea (especially *S. ramosus*,
440 Morzadec-Kerfourn, 1977), increasing presence of heterotrophic *S. quanta* with cysts of *P.*
441 *dalei* from 1.2 ka BP (limit C) may indicate the existence of stratified high productivity
442 conditions (Howe et al., 2010). In summary, the winter horizontal thermohaline front may
443 thus be identified at 3.3 ka BP based on the pronounced disconnection of oceanic and shelf
444 waters, the mid-shelf being characterized by enhanced stratification under increasing winter
445 fluvial discharges, with a trophic change at 1.2 ka BP resulting from increasing nutrient
446 bioavailability in surface waters.

447

448 **5.2. Atlantic Meridional Overturning Circulation and subpolar gyre** 449 **dynamics through the Holocene**

450 a. The 5.9 ka BP limit: evidence of strong oceanic re-organization

451 The north-eastern Atlantic is a key climatic area requiring careful attention, particularly with
452 regard to NAC vigour. This branch of the North Atlantic Sub-Polar Gyre (SPG; Sutton and
453 Allen, 1997) affects the Atlantic Meridional Overturning Circulation (AMOC) by varying
454 poleward heat transport intensity over time (Carton and Hakkinen, 2011). Some recently
455 published data made it possible to synthesize the long-term Holocene trend considering
456 AMOC dynamics (Figure 6). AMOC strength and SST south of Iceland were maximal until 6
457 ka BP (e.g., Eynaud et al., 2018; Ayache et al., 2018) before slowly decreasing (as shown by
458 the general decline in bottom flow strength: Kissel et al., 2013). This breakdown in North
459 Atlantic dynamics associated with hydrological reorganization occurred synchronously with
460 the 5.9 ka BP limit previously discussed for the CBT-CS11 core and resulting from the
461 slowdown of the RSL rise and the stabilization of estuarine banks. The final collapse of the
462 Laurentide Ice Sheet (Dyke, 2004; Kaplan and Wolfe, 2006; de Vernal and Hillaire-Marcel,
463 2006) implies the start of the Labrador Sea convection (minimum of sea-ice concentrations in
464 the eastern Fram Strait, northern Baffin Bay and Labrador Sea at 6 ± 0.5 ka BP, de Vernal et
465 al., 2013), thus impacting the AMOC through reduced poleward heat transport to the Nordic
466 Seas, and then contributing to the establishment of the modern AMOC (Hoogakker et al.,
467 2011; Ayache et al., 2018). Simultaneously, reduced summer SSTs in the north-eastern
468 Atlantic (MD95-2002 core; Zumaque et al., 2017; Figure 6) reflect the half-cycle of the
469 precessional signal implying decreasing summer insolation at 65°N for 9 kyrs (e.g., Berger
470 and Loutre, 1991; Ayache et al., 2018).

471
472
473
474
475
476
477
478
479
480
481
482
483
484
485
486
487
488
489
490
491
492
493
494
495
496
497
498
499
500
501
502
503
504

b. Eastern North Atlantic Central Water signature

Superimposed on this long-term RSL rise, AMOC, and insolation trends, North Atlantic SPG dynamics can be reconstructed at a sub-orbital timescale from marine sediment archives in the northern Atlantic Ocean (e.g., Giraudeau et al., 2010; Solignac et al., 2006, 2008; Zumaque et al., 2017; Ayache et al., 2018; Mojtahid et al., 2019). Millennial timescale events (Bond et al., 1997, 2001), as well as multi-decadal variability, related to internal modes of atmosphere-ocean teleconnection such as the “NAO-like” mechanism have exerted a control on the latitudinal position of westerly storm tracks (Sorrel et al., 2012; van Vliet et al., 2014; Goslin et al., 2018, 2019) and may have strongly impacted Atlantic gyre dynamics throughout the Holocene (Thornalley et al., 2009; Figure 6). Since the CBT-CS11 core was influenced by Eastern North Atlantic Central Waters (ENACW), which were themselves influenced by the NAC, Mojtahid et al. (2019) discussed the benthic $\delta^{18}\text{O}$ signal of *Cibicides refulgens* as a proxy for ENACW waters mainly responding to subpolar rather than subtropical gyre influences. To complement these interpretations and go further, we produced another series of $\delta^{18}\text{O}$ measures on the benthic foraminifera *Ammonia falsobeccarii* (Figure 6). Higher isotopic values on both species, here highlighting mainly higher salinities (such as tropical ENACW today; Voelker et al., 2015; Figure 6), match the density anomalies at sub-thermocline depths recorded in the southern Iceland basin (Thornalley et al., 2009; Figure 6). However, the two benthic isotopic records diverge at 3.3 ka BP (limit B; Figure 6), with the *C. refulgens* signature being characterized by a shift towards a new oscillating salinity state with heavier values after 3.3 ka BP. Mojtahid et al. (2019) interpreted this shift as an overall cooling state that occurred under the establishment of the winter thermohaline front (Figure 6). Since *C. refulgens* is an epibenthic/epiphyte species, we hypothesize that it may reflect an isotopic signature more characteristic of the surface (being transported by currents after first becoming attached to littoral plants) and thus a cooling related to fluvial water advections being plated to the coast up to the 100 m isobath. *A. falsobeccarii*, which is part of the surficial infauna, would calcify in equilibrium with poral waters, being less influenced by seasonal surface conditions related to river plumes and more by polar (ENACWP) than tropical (ENACWT) oceanic signatures (cf. Figure 1a). The *C. refulgens* isotopic record confirms the 3.3 ka BP limit as the main time when the modern winter thermohaline front was established (Mojtahid et al., 2019). *A. falsobeccarii* will be used as a SPG dynamic index in the following discussion (Figure 7).

505
506
507
508
509
510
511
512
513
514
515
516
517
518
519

c. Subpolar gyre dynamics and Bond events

As a second step, we compared the *A. falsobeccarii* record with Ice-Rafted Debris (IRD) data in the North Atlantic (Bond et al., 2001; Figure 7). From the mean value of both datasets, we established an anomaly scale: red (less IRD–weaker SPG, with a more pronounced ENACWT signature) and blue (more IRD under stronger EGC–stronger SPG, with a greater influence of ENACWP at our studied site and of the NAC in the Nordic Seas). The two signals show a good concordance, with enhanced SPG strength at times of peaks in IRD, especially across Bond events 4, 2 and 1 (Figure 7). These three major intervals (6.4–5.1, 3.3–2.7, and 1.6–1.2 ka BP) were coded with blue bands for the following discussion and the red/blue scale (SPG dynamics) based on the *A. falsobeccarii* $\delta^{18}\text{O}$ oscillating signal (cf. Figure 7) was placed in parallel with other proxies to improve the mechanistic understanding of climatic and hydrographic changes and related environmental impacts over the last 7 kyrs (Figures 8 to 10).

5.3. Oceanic versus continental influences on the Bay of Biscay shelf

The BoBy exhibits three kinds of hydrographic regime depending on the bathymetry: the abyssal plain, the continental slope and the northward widening continental shelf reaching 160 km on the Armorican shelf. The BoBy is thus influenced by large-scale oceanic circulation (which we will refer to as “oceanic influence”) and local forcing implying seasonal wind regimes as well as river discharges and run-off (which we will refer to as “continental influence”). It is worth keeping in mind that our observations filter the mesoscale and interannual variability to depict multi-decadal scenarios of environmental forcing and related impacts.

530

a. From 7 to 5.9 ka BP (~Early–Middle Neolithic)

During this period, pollen concentrations were higher than dinocyst ones and seasonal synchronization between pollen production and river transport is assumed because of high pollen fluxes (Figures 3d and 9). These may correspond to high arboreal pollination (higher summer insolation at 65°N) having been synchronous with fluvial discharges of the main rivers, thus implying higher precipitations during spring. In terms of sediment facies, we suggest that the generally coarser sedimentation (Zr/Al ratio, D50 CaCO₃ free; Mojtahid et

538 al., 2019), resulting from spring fluvial currents, took over the winter supply of fine material
539 by fluvial turbid plumes. This hypothesis appears to be supported by the overall coherence we
540 observe between grain-size tracers and summer SSTs reconstructed in the Bay of Biscay (core
541 MD95-2002; Figure 8). Until 5.9 ka BP, stronger occurrences of the cosmopolitan-oceanic *O.*
542 *centrocarpum* species, **suggested here** as a potential tracer for the NAC (Rochon et al., 1999),
543 than occurrences of *L. machaerophorum* (ratio “*O. centrocarpum* / *L. machaerophorum*” on
544 Figure 9), would reflect an increasing strength of the NAC at a time of stronger AMOC (e.g.,
545 Ayache et al., 2018). We **further** suggest that stronger humidity through the NAC may have
546 amplified seasonal continental humidity in Western France during the hypsithermal.
547 Therefore, in a high boreal summer insolation context (Holocene Thermal Maximum; e.g.,
548 Renssen et al., 2012), strong pollination of trees coupled **with** spring precipitations would be
549 responsible for higher arboreal pollen fluxes to the **shelf**. We entitled this configuration
550 “summer-prevailing mode” and suggest that a north-west to south-east shelf residual
551 circulation was prevalent within the BoBy (Figures 8 and 11). At that time of still rapid RSL
552 rise (Garcia-Artola et al., 2018), southward residual shelf currents may have dominated sea-
553 surface circulation in the **BoBy**.

554

555 b. From 5.9 to 3.3 ka BP

556 At 5.9 ka BP, the reduced accommodation space on the **shelf**, as well as the stabilization of
557 fluvial environments, favoured the development of alluvial plains and allowed the ripisylve to
558 progressively colonize riverbanks (limit at 5.7 ka BP identified by Cyprien, 2002). This
559 period of valley alluviation (increasing *Alnus* and *L. machaerophorum* percentages; Figure 9)
560 corresponds to a still active poleward heat transport to the Nordic Seas via the NAC (as
561 shown by the **persistent** high percentages of *O. centrocarpum*; Figure 8) and the rise of
562 *Corylus* and *Betula* under **increasingly** fresher and wetter climate conditions. Thanks to the
563 development of riparian hydrophilous shrublands along freshwater bodies, the stabilization of
564 fluvial systems (i.e., **development of vegetation on riverbanks and their fixation**) may have
565 implied: i) reduced sedimentation rates to the **shelf** by retaining solid and dissolved river
566 inputs (Figure 9), and ii) increased brackish waters in coastal waters (major drops in salinity)
567 as observed through *L. machaerophorum* cyst proliferation (Figure 9).

568

569 Two sub-periods can be identified within this time interval:

570

- 571 • 5.9 to 4 ka BP (~Recent–Late Neolithic): The sustained elevated abundances of *O.*
572 *centrocarpum* and **relatively** coarse sedimentation may suggest mixed oceanic-
573 continental influences with a non-oriented shelf residual circulation, **referred to here as**
574 “autumn-prevailing mode” (Figures 8 and 11). This mode would have especially
575 prevailed until 4 ka BP (equivalent values of neritic-oceanic and *L. machaerophorum*
576 concentrations and fluxes, high tree pollen grain percentages; Figure 9). This period
577 would correspond to the settlement and evolution of Recent and Late Neolithic coastal
578 societies on the fringes of coastal zones (e.g., Molène archipelago; Pailler and Nicolas,
579 2019).
- 580
- 581 • 4 to 3.3 ka BP (~Early–Middle Bronze Age): This interval **fits** within the larger 4–2 ka
582 BP interval identified in Figure 5 (yellow band). This latter also corresponds to a
583 peculiar interval of generally higher winter SST and SSS (2 to 3 psu higher-than-
584 average) within the MD95-2002 slope core (yellow band on Figure 6), **which was**
585 synchronous with the strongest *L. machaerophorum* occurrences (Figure 9) and
586 generally weaker SPG dynamics (Thornalley et al., 2009; Figures 6 and 9).
587 **Additionally**, a shift at 4 ka BP from **prevalently** positive to **prevalently** negative
588 NAO-like conditions until 2 ka BP was suggested from the study of a lake sediment
589 record from south-western Greenland (Olsen et al., 2012; Figure 9). The long-term
590 phase of recurrent negative NAO-like conditions may have resulted in an enhanced
591 East Greenland Current and/or in some melting of the Greenland Ice Sheet according
592 to Orme et al. (2018) who identified a major long-term SST cooling south of the
593 Iceland Basin over the 4–2 ka BP interval. Our data **tell** a more complex story for this
594 latter 4–2 ka BP interval and **make it possible** to divide it in three sub-periods. The 4–
595 3.3 ka BP period constitutes its first phase and is characterized by negative NAO-like
596 recurrent modes. Poleward flows have been thoroughly studied (Pingree and Le Cann,
597 1989; Koutsikopoulos and Le Cann, 1996) and are known to occur frequently within
598 the BoBy, pulsing during the autumn and winter seasons (Charria et al., 2013). This
599 along-slope circulation (IPC; top 350 m of the water column; Figure 1b) implies
600 seasonal warmer conditions extending up to the Armorican slope, and it has been
601 suggested that, **today**, southerly winds represent the **main** contribution to the IPC
602 intensification over the upper slope and outer shelf, generating anomalously high
603 winter SSTs (e.g., Pingree and Le Cann, 1992a,b; Le Cann and Serpette, 2009; Garcia-
604 Soto and Pingree, 2012). Here, we thus suggest that, between 4 and 3.3 ka BP,

605 prevalent southerly winds may have promoted a northward IPC, resulting in higher
606 winter SSTs in the north-eastern Atlantic Ocean (MD95-2002; Figure 9). The highest
607 *I. aculeatum* percentages recorded within core MD95-2002 during this time interval
608 (Zumaque et al., 2017; Figure 5) reinforce the hypothesis of a major advection of
609 subtropical waters during this interval. This context may have promoted major winter
610 precipitation and thus major repeated flood events **over the** Loire riverbanks during the
611 winter seasons. It is **noteworthy** that Delaine et al. (2015), who studied the Loire
612 valley infilling near Nantes during the Holocene, reported a period of high erosional
613 regime and/or intense reworking denoting high hydrodynamics of the Loire **River**
614 **from ~ 5.8 to 2.1 ka BP. In addition**, a synthesis on the Loire **showed** a peak frequency
615 and/or magnitude of floods between 4.4 and 3.5 ka BP (Val d'Orléan; Arnaud-Fassetta
616 et al., 2010), **concomitant** with our observation.

617
618

619 c. From 3.3 to 1.2 ka BP

620 This **period was** characterized by a strong drop **in** Greenland air temperatures (Vinther et al.,
621 2006; Figure 8), large global temperature anomalies (Marcott et al., 2013; Figure 8), as well
622 as increasing annual precipitation and decreasing atmospheric temperature seasonality as
623 shown by pollen-based climate reconstructions conducted in north-western France (Core
624 VK03-58bis; Naughton et al., 2007; Figure 1b). At 3.3 ka BP, this change in precipitation
625 resulted in major winter river discharges (Stéphan et al., 2015) and **a large decrease in** oceanic
626 influence (major decline of *O. centrocarpum* percentages) in BoBy shelf waters. Finer
627 sediments (Figure 8) thus correspond to winter advection of fine sediments and spring
628 deposition under hypopycnal currents (similar to the present-day configuration: Charria et al.,
629 2013). The establishment of the winter horizontal thermohaline front is obvious here at 3.3 ka
630 BP and this configuration was **named** the “winter-prevailing mode” (Figures 8 and 11).

631 The 4–2 ka BP interval of prevalent negative NAO-like conditions is **interrupted** by the 3.3–
632 2.8 ka BP interval (Bond event 2; Figures 8 and 9) during which persistent positive NAO-like
633 conditions occurred, accompanied **by** enhanced SPG strength, decreased influence of the
634 warm and salty poleward current (lower winter SST/SSS offshore), and strengthened northern
635 Atlantic westerly storminess (Goslin et al., 2018; Figure 9). Regionally, this latter period
636 (Middle to Late Bronze Age) was characterized by a **scarcity of** coastal archaeological
637 remains. Indeed, it is generally accepted that the harsh meteorological conditions caused by
638 this period of climatic deterioration, accompanied with widespread dune-sand invasions of

639 coastal areas (e.g., Tisdall et al., 2013; van Vliet et al., 2016), may have caused the
640 withdrawal of coastal societies from the shores during the winter season or even permanently
641 (Stéphan et al., 2013, 2018). Among other adaptive possibilities, this may have encouraged
642 some populations to turn more towards land cultivation rather than exploitation of marine
643 resources (although salt producers were probably also farmers or herders). This is suggested
644 by the decreasing occurrences of *Alnus* and *Corylus* pollen grains in our data (and further
645 emphasized by the ratio of *Corylus* to *Quercus* (explained in Table 2) in Figure 9), which may
646 reflect major phases of upland clearance (Figure 9). The anthropogenic origin of this pollinic
647 observation is also indicated by the fact that no comparable shifts appeared during either
648 Bond event 4 or 1 while, on the contrary, both pollinic tracers (*Alnus*, *Corylus*) tended to
649 increase (Figure 9). Accounting for the synchronous trend of increasing sedimentation rates
650 (Figure 9), the drops in *Alnus* and *Corylus* percentages around 3.3–2.8 ka BP, while *Betula*
651 percentages remain stable, could indicate an anthropogenic impact on the landscape, with
652 preferential human selection of alluvial taxa in a context of landscape opening (a continuing
653 decreasing trend of arboreal pollen percentages following the increase of Poaceae as well as
654 of *Plantago lanceolata*; Figure 4b).

655

656 d. From 1.2 ka BP onwards

657 From 1.2 ka BP, which also corresponds to the end of Bond event 1, a sharp shift was
658 observed in both pollen and dinocyst communities (Figure 10). Cultivated, ruderal and
659 adventive plants clearly indicate massive landscape opening after this point (Figure 10). The
660 increase in the area under cultivation and pasture was thus established from the Middle Ages,
661 as previously noted (Barbier and Visset, 1997; Cyprien, 2002; Joly and Visset, 2009; David,
662 2014). At this time, the increase in sedimentation rates may thus have resulted from rainwater
663 runoff over bare watersheds. The human imprint on coastal wetlands also became strong,
664 especially for drainage or water intakes (Joly and Visset, 2009).

665 Increasing concentrations of *S. quanta*, a heterotrophic taxon, and of cysts of *P. dalei* (Figure
666 10) could be explained by an increase in the supply of nutrients to the shelf, most likely
667 provoked by the reduction of the forest cover and the subsequent increase of soil erosion and
668 continentally derived organic matter. This may indicate the existence of stratified high
669 productivity conditions (Howe et al., 2010). Indeed, cysts of *P. dalei* increase when upper
670 water salinities are reduced throughout the year as a result of increasing: i) freshwater riverine
671 inputs (Zonneveld et al., 2013) and ii) phosphate concentrations within the upper water
672 column (Zonneveld et al., 2012). Because *Lingulodinium polyedrum* cyst formations are

673 favoured in cultures in a media replete in phosphate levels (Figuroa and Bravo, 2005), the
674 massive nutrient, and especially phosphate, influx from 1.2 ka BP would contribute to
675 explaining the sharp drop in *Lingulodinium machaerophorum* occurrences. At that time, it
676 should also be noted that the highest concentrations of diversified dinocysts (without *L.*
677 *machaerophorum*: ~5,000 cysts/cm³; Figure 3b and 5) are recorded. The same trophic re-
678 organization of coastal water bodies has recently been described in the Bay of Brest, though
679 in much higher proportions, with sharp drops of *L. machaerophorum* percentages related to
680 intensive agriculture practices after World War II (Lambert et al., 2018).

681

682 **5.4. Understanding western European river floods**

683 a. Effects of climate-driven factors on anthropogenic palynological evidence

684 As a first general observation, the first clear retreat of mixed temperate forest was recorded
685 between 4.5 and 4 ka BP, indicating the beginning of the landscape opening and onset of
686 inland agro-pastoral practices (as shown by the presence of ruderal plants such as *Rumex* and
687 *P. lanceolata* accompanied by first low *Cerealia* occurrences, Figure 10). This is consistent
688 with other pollinic studies carried out in north-western France (e.g., Gaudin, 2004; David,
689 2014; Fernane et al., 2014, 2015), i.e., with the transition from the Neolithic to the Bronze
690 Age cultural periods (Figure 10). The next major step in landscape opening dynamics
691 occurred at the Bronze to Iron Age transition, shown well by the increase of ruderal and
692 cultivated plants, as well as by a higher “dinocyst (without *L. machaerophorum*) to pollen”
693 ratio (Figure 10). The rise of this ratio is probably based on two non-exclusive factors: i) a
694 higher dinocyst productivity induced by nutrient enrichment of coastal waters, and ii) a
695 smaller contribution of the strongest tree pollinators to the pollen assemblages induced by the
696 clearing of regional woodlands.

697 It is interesting to observe, however, that the most representative indices of anthropogenic
698 impacts increase during periods of weakened SPG dynamics (or higher subtropical influence,
699 red/blue scale on Figure 10). In other terms, palynological tracers of anthropic activity appear
700 closely associated with more favourable climate conditions that allowed their transport and
701 record to be left in marine sediments. This hypothesis is further confirmed by the fact that
702 *Echinidinium* spp. percentages follow a pattern equivalent to the one followed by ruderal
703 plants or Poaceae (Figures 4a and 10). The fluvial (or river-plume) sensitive nature of
704 *Echinidinium* spp. (Zonneveld et al., 2013) confirms that strengthened nutrient-enriched river
705 discharges occurred during time intervals characterized by weakened SPG activity. This

706 illustrates the difficulty of **accurately tracing past** human dynamics using pollen indicators of
707 anthropisation within marine sediments. Indeed, their occurrences may first be the expression
708 of higher precipitation capable of transporting heavy pollen grains to the sea. These indices
709 nonetheless seem to adequately depict the main trends of anthropogenic impacts in regional
710 watersheds from the start of the Bronze Age and later, as illustrated by **the regular Poaceae**
711 **profile (dotted line in Figure 10: theoretical Poaceae trend).**

712

713 b. An atypical signal of arboreal expansion during the 1.8–1.2 ka BP interval

714 When looking at **the general Poaceae trend** since the start of the Bronze Age (Figure 10), it is
715 tempting to connect the arboreal rise between 1.8 and 1.2 ka BP with a major human decline
716 **that coincided** with the Roman period and transition to the start of the Middle-Ages (Lambert
717 et al., **pers. comm.**, for the Bay of Brest). For instance, working on a coastal sedimentary
718 archive (southern edge of the Armorican Massif), Joly and Visset (2009) observed the
719 reappearance of the oak during the Gallo-Roman period (as also observed in the Mayenne and
720 Loire valleys, Barbier and Visset, 1997; Ouguerram and Visset, 2001; Cyprien, 2002), and
721 suggested a link with possible strategies of forest management in reaction to forest over-
722 exploitation during the Iron Age. However, the sharp increase in sedimentation rates at 1.8 ka
723 BP (Figure 10) that we attributed to human-induced soil erosion, **suggests** hydrographic
724 changes could be responsible for this atypical arboreal re-increase.

725 Several phases of SPG strengthening took place within the 1.8–1.2 ka BP interval (major
726 climate deterioration of Bond event 1; Figure 10). This climatic context probably also had
727 **consequences for** the arboreal *versus* Poaceae signatures; tree pollen grains being better
728 preserved in marine sediments while, as previously discussed, **the Poaceae signature is**
729 **enhanced by stronger fluvial discharges.** The impact of oceanic *versus* river processes on tree
730 *versus* Poaceae occurrences and preservation **would also be clearer** in the context of an
731 already opened landscape. This may explain the strong Poaceae decline observed during Bond
732 event 1, but also the weaker ruderal signature observed during Bond event 2, while Bond
733 event 4 occurred in a period during the **Neolithic, when major forest clearings were not yet**
734 **observed.**

735 Interestingly, during the 1.8–1.2 ka BP interval, percentages of fluvial-sensitive
736 *Echinidinium* spp. taxa as well as **the dinocyst to pollen ratio were** characterized by sharp
737 drops, suggesting a small impact of river discharges to our study site. Also, a recent study
738 from Durand et al. (2018), carried out at the mouth of the Loire **River** for the Late Holocene,
739 discussed the influence of positive NAO-like configurations responsible for lower terrigenous

740 inputs to the sea **in a period known for** increased storminess. However, even if the absence of
741 anthropogenic indices and the peak in arboreal pollen grains may not result from human
742 causes (i.e., forest management, land abandonment in a context of wars or invasions), we
743 cannot exclude that this climate event could have had serious consequences for coastal and
744 inland societies because of storms and stronger humidity under recurrent positive NAO-like
745 conditions.

746

747 c. Factors required for major Holocene Loire **discharges**

748 Interestingly, major peaks of palynomorph fluxes (/drops of anthropogenic indexes), **make it**
749 **possible** to understand the environmental conditions required for increasing (/decreasing)
750 **fluvial discharges** from major north-western French rivers (Figure 9). During Bond events,
751 strong positive NAO-like configurations are known to favour increased precipitation and
752 storminess, then fostering fluvial discharges in north-western Europe (as **observed by Tréguer**
753 **et al., 2014, for the 1998–2013**-time interval in the Bay of Brest). The opposite is true during
754 negative NAO modes. Here, palynomorph fluxes (Figure 9) generally increased during
755 periods characterized by weakened SPG dynamics and prevalent negative NAO-like
756 conditions (Figure 9). This would imply that, at the location of the studied site (south
757 Brittany), sediment supply is more influenced by river systems **with** watersheds extending
758 southwards. The Loire **River**, and probably the Gironde, may thus largely explain our
759 palynological concentration/flux records. Higher palynomorph fluxes (dates **given** in red in
760 Figure 9) generally coincide with subtropical gyre strengthening and negative NAO-like
761 conditions. On the general “summer-prevailing”, “autumn-prevailing” and “winter-
762 prevailing” modes (Figure 8) linked with the long-term insolation trend (Berger and Loutre,
763 1991), **we can therefore superimpose** a millennial-scale mechanism implying SPG strength
764 coupled with natural atmospheric oscillations (Figure 11). Indeed, it has been demonstrated
765 that North Atlantic SPG response is strongly related to persistent NAO configurations even
766 though a large non-linearity exists regarding the NAO response to atmospheric forcing
767 (Lohmann et al., 2009). A steady weakening of the SPG was however found throughout the
768 integration of negative NAO modes in **a modelling study by** Lohmann et al. (2009), while
769 positive phases of the NAO strengthened the SPG with poleward advection of NAC waters.
770 This is notably due to the wind-stress implied by northern-located mean westerly storm tracks
771 (e.g., Giraudeau et al., 2010; Goslin et al., 2018). Stronger Loire **River discharges** from the
772 start of the Late Holocene would therefore represent a conjectural phenomenon of stronger
773 subtropical gyre influence under negative NAO-like modes. This latter scenario may have

774 been amplified by periods of solar minima (reduced solar activity or solar irradiance under
775 lower magnetic waves; Steinhilber et al., 2009; Figure 8). Indeed, during solar minima,
776 several observational **revealed** southward shifts of North Atlantic storm tracks towards central
777 to southern Europe (south of the 50°N) as well as an increase of associated precipitation and
778 flood frequency (e.g., de Jong et al., 2006, 2007; Costas et al., 2012; Laurenz et al., 2019). As
779 far as our data is concerned, **with** the exception of some events (**at** 5.9, 3.4 and 1.3 ka BP), the
780 correlation between solar forcing and palynomorph fluxes at a multi-decadal timescale is
781 **insufficiently** significant, but was convincingly discussed for the mouth of the Loire **River in**
782 **a previous study** (Durand et al., 2018).

783

784 **6. Conclusion**

785 Ecosystem resilience to natural hazards, as well as to human occupation or withdrawal from
786 the coast, **is a compelling issue** across the Holocene. In the present study, we took advantage
787 of the complex sedimentation context of the northern Bay of Biscay (BoBy) shelf, especially
788 marked by the dual influence of both oceanic currents derived from the North Atlantic
789 Current and winter fluvial discharges, to address several issues regarding the links between
790 natural climate modes (including Atlantic subpolar gyre and North Atlantic Oscillation
791 dynamics, storminess and floods) and the dynamics of terrestrial and marine ecosystems. Our
792 study may therefore help the archaeology community to understand major phases of
793 occupation or desertion of coastal sites on the **western French** coastal fringe, but also the
794 climate community to place the Loire floods as observed today in a broader spatio-temporal
795 context.

796 **The high-time resolution (~70 years on average) multi-proxy analysis on the CBT-CS11 mid-**
797 **shelf core revealed the complexity of the palaeohydrological and palaeoclimatic signals**
798 **recorded over the last 7 kyrs. At 5.9 ka BP, we identified major reorganizations of the**
799 **hydrological systems accompanying the stabilization of the sea-level rise and the slowdown**
800 **of the Atlantic Meridional Overturning Circulation. We also revealed repetitive**
801 **intensifications of the fluvial discharges, here mainly connected to the hydrological regimes**
802 **of the Loire River, and showed the links between these latter events and increased winter**
803 **precipitations during periods of enhanced subtropical gyre dynamics coupled with negative**
804 **NAO-like modes. Among these events, major ones occurred within the 4–2 ka BP interval**
805 **with probable repercussions for coastal societies from the Early Bronze and Iron Ages (access**
806 **to marine food resources in spring, flooding risks during winter). In addition, within the 4–2**
807 **ka BP interval, the 3.3 ka BP appeared as the establishment of the winter horizontal**
808 **thermohaline front in the BoBy shelf. Finally, we revealed major soil erosion and primary**
809 **productivity increase since 1.8 ka BP (Roman Period) and more specifically since 1.2 ka BP**
810 **(Early Middle Ages).**

811

812 **7. Acknowledgments**

813 Analysis benefited credits by a CNRS-INSU project HCOG2 (2013-2014) “*Forçages*
814 *climatiques Holocène et répercussions Côtières et Océaniques dans le Golfe de Gascogne*”
815 (ccord. A. Penaud) in the context of the LEFE-IMAGO research axis, and French ANR
816 HAMOC (ANR-13-BS06-0003). ¹⁴C dates were mainly obtained thanks to French national
817 ARTEMIS ¹⁴C AMS facilities (2013, 2014, 2015, 2019). We would like to thank Oanez
818 Lebeau (IUEM, Brest) from the “*Pôle Spectrométrie Océan*” (IUEM, CNRS, IFREMER) for
819 her help with isotope analyses. We also thank the Ifremer for core acquisition and laboratory
820 facilities, especially Samuel Toucanne. Authors thank the ZABrI (“*Zone Atelier Brest Iroise*”,
821 CNRS-INEE) and the ArMeRIE program funded by the UBO (Univ Brest) for fruitful
822 interdisciplinary exchanges about human dynamics and Holocene paleoenvironments. **Raw**
823 **data (sedimentological and palynological data) are available as online supplementary material**
824 **(Data in Brief) or by contacting the first author (aurelie.penaud@univ-brest.fr).**

825

826 **8. Table caption**

827 **Table 1:** CBT-CS11 AMS-¹⁴C dates. In black, dates previously published in Mojtahid et al.
828 (2018). In bold and red: new dates from ARTEMIS received in March 2019. Grey cells
829 represent levels averaged for the final age model. Dates in italic (with the annotation « * »)
830 were rejected for the final age model (Figure 2).

831

832 **Table 2:** This table gathers CBT-CS11 data discussed in this study and describes the way data
833 were obtained (methodology) and can be interpreted. It is worth noting that a **Data in Brief**
834 paper complementary to this study describes multivariate analysis on which some taxa groups
835 or ratios here listed were established.

836

837 **9. Figure captions**

838 **Figure 1: a)** Geographical map of the “HAMOC” database subdivisions (provinces) with the
839 location of the selected sedimentary records for the HAMOC synthesis (Eynaud et al., 2018;
840 Ayache et al., 2018) and the additional superimposed studied site CBT-CS11. **b)** Map
841 illustrating the general surface circulation of the Bay of Biscay (Koutsikopoulos and Le Cann,
842 1996) and the extent of the Loire and Gironde catchment areas. Are indicated the locations of
843 the CBT-CS11 core (studied site) and of the other cited cores in the text: VK03-58bis core
844 (Naughton et al., 2007); A core (Lambert et al., 2019); MD95-2002 core (Zumaque et al.,
845 2017). Map performed using the online EMODnet Portal for Bathymetry
846 (<http://www.emodnet-bathymetry.eu/>) and adapted from Mojtahid et al. (2019).

847

848 **Figure 2:** Age model for the CBT-CS11 core. **a)** Age-Depth plot of all dates obtained on the
849 core allowing to address three main trends in sedimentation rates. The plot is represented in
850 parallel with: relative sea level (RSL) heights for southern Brittany from García-Artola et al.
851 (2018), northern Europe (western Denmark) paleo-temperatures as reconstructed by the
852 Aeolian Sand Influx (ASI) (Goslin et al., 2018), Bond Events as reconstructed through
853 hematite-stained quartz percentages with stacked North Atlantic Ocean cores (Bond et al.,
854 2001) and Total Solar Irradiance (TSI; Steinhilber et al., 2009). Blue horizontal bands
855 represent stacked Eastern European Atlantic Storm Events (Pouzet et al., 2018) while dark
856 blue vertical lines to the right only point to the southern Brittany paleostorminess record (Yeu
857 island; Pouzet et al., 2008). The superimposition of both information allows to establish the

858 vertical storm scale also shown in Figures 8 and 9. **b)** Final age model established using the
859 *Bchron* package in R version 3.5.1. **c)** Cultural subdivisions for western Brittany.

860

861 **Figure 3:** CBT-CS11 palynological data against depth (cm): Diversity indexes (Table 2) are
862 drawn in blue for dinoflagellate cysts (**a**, in parallel with percentages of the major species
863 *Lingulodinium machaerophorum*) and in green for pollen assemblages (**c**, in parallel with
864 percentages of *Quercus* and Total Trees); Concentrations (in linear scale) and fluxes (in
865 logarithmic scale) for dinocysts (**b**) and pollen grains (**d**). The yellow horizontal band
866 underlines the atypical elevated signatures (percentages, concentrations, fluxes) of *L.*
867 *machaerophorum*. A to C horizontal dotted lines consist in the main limits between the four
868 palynozones discussed in the manuscript. **To the left, all radiocarbon dates are represented in**
869 **Cal BP with rejected dates in italic-grey and selected dates for age model in bold-red.**

870

871 **Figure 4:** CBT-CS11 palynological data against depth (cm): major taxa occurring with values
872 higher than 2% in palynological assemblages. **a)** dinoflagellate cyst (dinocyst) and **b)** pollen
873 assemblages. Palynozones CBT 1 to CBT 5 are shown with CBT 5 being included in the
874 probably reworked part of the top 60 cm of the studied core (grey band). A to C horizontal
875 dotted lines consist in the main limits between the four palynozones discussed in the
876 manuscript. To the left, all radiocarbon dates are represented in Cal BP with rejected dates in
877 italic-grey and selected dates for age model in bold-red.

878

879 **Figure 5:** Nearshore-offshore dinocyst communities plotted in age (Cal years BP) from
880 coastal (A core; Lambert et al., 2019; green code: line or full color), shelf (CBT-CS11 studied
881 core; pink code: line or full color) to full-oceanic (MD95-2002 core; Zumaque et al., 2017;
882 purple full color) waters in the northern Bay of Biscay. Data are expressed in percentages
883 considering all dinocyst taxa for *Lingulodinium machaerophorum* percentages **only, and**
884 **without considering this latter species in the main dinocyst sum for all other taxa percentages.**
885 Yellow horizontal band underlines the atypical elevated signatures (percentages,
886 concentrations) of *L. machaerophorum*. A to C horizontal dotted lines consist in the main
887 limits between the four palynozones discussed in the manuscript.

888

889 **Figure 6:** Long-term Holocene insolation trends at 65°N (Berger and Loutre, 1991) in parallel
890 with seasonal Sea-Surface Temperature (SST) and Sea-Surface Salinity (SSS) reconstructions
891 in the north-eastern Atlantic Ocean (MD95-2002 core; Zumaque et al., 2017), as well as

892 qualitative estimates of summer SST South of Iceland (Orme et al., 2018; Eynaud et al.,
893 2018). North Atlantic SubPolar Gyre (SPG) millennial-scale dynamics (density anomalies at
894 sub-thermocline depths recorded in the southern Iceland Basin) are based on temperature and
895 salinity reconstructions of the surface subpolar North Atlantic (Thornalley et al., 2009) and
896 are compared with $\delta^{18}\text{O}$ signatures of *Cibicides refulgens* and *Ammonia falsobeccarii* benthic
897 foraminifera. $\delta^{18}\text{O}$ SW (Sea Water) for isotope signatures of Northeast Atlantic water masses
898 (Voelker et al., 2015). ENACW: Eastern North Atlantic Central Waters (P for Polar and T for
899 Tropical). Yellow horizontal band underlines the atypical elevated occurrences of *L.*
900 *machaerophorum* (cf. Figure 5). A to C horizontal dotted lines consist in the main limits
901 between the four palynozones discussed in the manuscript.

902

903 **Figure 7:** Bond Event (BE) curve (Hematite-stained quartz grain percentages; Bond et al.,
904 2001) in parallel with $\delta^{18}\text{O}$ acquired on *Ammonia falsobeccarii* benthic foraminifera. From
905 mean values of both datasets (i.e. locations of the coloured scale), a code based on
906 positive/negative anomalies has been established in reference with the average of the
907 considered dataset: Red (less Ice-Rafted Debris: IRD or weaker Sup-Polar Gyre: SPG) *versus*
908 blue (more IRD or stronger SPG). Grey horizontal bands underline main common periods of
909 stronger SPG–IRD between both proxies, and blue inserts to the right point to the selected
910 intervals that will be drawn on Figures 8 to 10, especially representative of the *A.*
911 *falsobeccarii* $\delta^{18}\text{O}$ stronger negative anomalies (Bond events 4, 2 and 1). ENACW: Eastern
912 North Atlantic Central Waters (P for Polar and T for Tropical). A to C horizontal dotted lines
913 consist in the main limits between the four palynozones discussed in the manuscript.

914

915 **Figure 8:** Sedimentological (grain-size analyses and Zr/Al XRF ratio) as well as selected full-
916 oceanic dinocyst data (percentages without *L. machaerophorum* in the main sum, and
917 concentrations) plotted in age for the CBT-CS11 core, in parallel with NGRIP oxygen
918 isotopes (Vinther et al., 2006) to the left as well as Bond events (Bond et al., 2001) and Total
919 Solar Irradiance (TSI; Steinhilber et al., 2009) to the right of the diagram. Note also
920 additional data from the MD95-2002 slope core (Zumaque et al., 2017): dinocyst-based
921 summer Sea-Surface Temperature (SST) as well as qualitative major occurrences of *O.*
922 *centrocarpum* and *S. mirabilis* (depicted in percentages in Figure 5). Blue horizontal bands
923 are representative of Bond events 4, 2 and 1 from the base to the top of the core. Yellow
924 horizontal band underlines the atypical elevated occurrences of *L. machaerophorum* (cf.

925 Figure 5). A to C horizontal dotted lines consist in the main limits between the four
926 palynozones discussed in the manuscript.

927

928 **Figure 9:** CBT-CS11 sedimentation rates and selected palynological data (cf. Table 2), in
929 parallel with North Atlantic Oscillation (NAO) data as interpreted from the NAO index
930 (Trouet et al., 2009; Olsen et al., 2012), northern Europe storminess (Goslin et al., 2018; ASI:
931 Aeolian Sand Influx), and winter Sea-Surface Temperature (SST) in the northern Bay of
932 Biscay (Zumaque et al., 2017). Blue horizontal bands are representative of Bond events 4, 2
933 and 1 from the base to the top of the core. Yellow horizontal band underlines the atypical
934 elevated occurrences of *L. machaerophorum* (cf. Figure 5). A to C horizontal dotted lines
935 consist in the main limits between the four palynozones discussed in the manuscript. IPC:
936 Iberian Poleward Current. NAC: North Atlantic Current.

937

938 **Figure 10:** Selected palynological information from the continent (pollen) and marine
939 (dinocyst) compartments from the CBT-CS11 core exclusively, addressed in parallel with
940 sedimentation rates and Dinocyst *versus* Pollen ratios (cf. Table 2). Blue horizontal bands are
941 representative of Bond events 4, 2 and 1 from the base to the top of the core. Yellow
942 horizontal band underlines the atypical elevated occurrences of *L. machaerophorum* (cf.
943 Figure 5). A to C horizontal dotted lines consist in the main limits between the four
944 palynozones discussed in the manuscript. Cf. Figure 2 for cultural subdivisions in full text.

945

946 **Figure 11:** Synoptic approach of main hydrographic and climatic influences that prevailed at
947 the western French coast scale. Superimposed on the “winter”, “autumn” and “winter” modes
948 linked with the long-term insolation trend, millennial and infra-millennial mechanisms imply
949 SubPolar Gyre (SPG) strength coupled or forced by natural atmospheric oscillations such as
950 the North Atlantic Oscillation (NAO) and solar activity. IPC: Iberian Poleward Current;
951 ENACW: Eastern North Atlantic Central Water; NAC: North Atlantic Current; SST: Sea-
952 Surface Temperature.

953

954 **10. References**

- 955 Andreieff, P., Boillot, G., Buge, E., Genesseeux, M., 1969. La couverture
956 sédimentaire tertiaire à l'Ouest et au Sud-Ouest du Massif Armoricaïn. Bulletin du BRGM (2)
957 – IV. Géologie générale IV (4), 23-37.
958
- 959 Arnaud-Fassetta, G., Carcaud, N., Castanet, C., Salvador, P.-G., 2010. Fluviale
960 palaeoenvironments in archaeological context: geographical position, methodological
961 approach and global change-hydrological risk issues. Quaternary International 216, 93-117.
962
- 963 Ayache, M., Swingedouw, D., Mary, Y., Eynaud, F., Colin, C., 2018. Multi-centennial
964 variability of the AMOC Over the Holocene: A New Reconstruction Based on Multiple
965 Proxy-derived SST Records. Global and Planetary Change 170, 172-189.
966
- 967 Barbier, D., Visset, L., 1997. Logn, a peat bog of European ecological interest in the Massif
968 Armoricaïn, western France: bog development, vegetation and land-use history. Vegetation
969 History Archaeobotany 6, 69-77.
970
- 971 Berger, A., Loutre, M.F., 1991. Insolation values for the climate of the last 10 million years.
972 Quaternary Science Reviews 10 (4), 297-317.
973
- 974 Bond, G., 1997. A Pervasive Millennial-Scale Cycle in North Atlantic Holocene and Glacial
975 Climates. Science 278, 1257-1266.
976
- 977 Bond, G., Kromer, B., Beer, J., Muscheler, R., Evans, M.N., Showers, W., et al., 2001.
978 Persistent Solar Influence on North Atlantic Climate During the Holocene. Science 294,
979 2130-2136.
980
- 981 Bourillet, J.-F., Zaragosi, S., Mulder, T., 2006. The French Atlantic margin and deep-sea
982 submarine systems. Geo-Mar. Lett. 26 (6), 311-315.
983
- 984 Carton, J.A., Hakkinen, S., 2011. Introduction to: Atlantic Meridional Overturning
985 Circulation (AMOC). Deep-Sea Res. II Top. Stud. Oceanogr. 58 (17), 1741-1743.
986
- 987 Castaing, P., Allen, G.P., 1981. Mechanisms controlling seaward escape of suspended
988 sediment from the Gironde: A macrotidal estuary in France. Marine Geology 40(1), 101-118.
989
- 990 Castaing, P., Froidefond, JM, Lazure, P, Weber, O, Prud'homme, R, Jouanneau JM, 1999.
991 Relationship between hydrology and seasonal distribution of suspended sediments on the
992 continental shelf of the Bay of Biscay. Deep Sea Research Part II: Topical Studies in
993 Oceanography 46(10), 1979-2001.
994
- 995 Charria, G., Lazure, P., Le Cann, B., Serpette, A., Reverdin, G., Louazel, S., et al., 2013.
996 Surface layer circulation derived from Lagrangian drifters in the Bay of Biscay. Journal of
997 Marine Systems 109-110.
998
- 999 Costas, S., Jerez, S., Trigo, R.M., Goble, R., Rebêlo, L., 2012. Sand invasion along the
1000 Portuguese coast forced by westerly shifts during cold climate events. Quaternary Science
1001 Reviews 42, 15-28.
1002

1003 Costoya, X., Fernandez-Novoa, D., de Castro, M., Santos, F., Lazure, P., Gomez-Gesteira,
1004 M., 2016. Modulation of sea surface temperature warming in the Bay of Biscay by Loire and
1005 Gironde Rivers. *Journal of Geophysical Research - Oceans* 121, 966-979.
1006

1007 Cyprien, A.L., 2002. Chronologie de l'interaction de l'homme et du milieu dans l'espace
1008 central et aval de la Loire (Ouest de la France). Thèse doctorat, Université de Nantes, Tome I,
1009 183 pp ; Tome II, 75 pp.
1010

1011 Dale, B., 1996. Dinoflagellate cyst ecology: modeling and geological applications. In: J.
1012 Jansonius and D.C. McGregor (Editors), *Palynology: principles and applications*, Vol. 3.
1013 AASP Foundation, Salt Lake City, 1 249-1 275.
1014

1015 Dale, B., Thorsen, T. A., Fjellså, A., 1999. Dinoflagellate cysts as indicators of cultural
1016 eutrophication in the Oslofjord, Norway. *Estuarine, Coastal and Shelf Science* 48, 371-382.
1017

1018 David, R., 2014. Modélisation de la végétation holocène du Nord-Ouest de la France :
1019 Reconstruction de la chronologie et de l'évolution du couvert végétal du Bassin parisien et du
1020 Massif armoricain. Thèse doctorat, université de Rennes I, 284 pp.
1021

1022 Debret, M., Bout-Roumazielles, V., Grousset, F., Desmet, M., McManus, J.F., Massei, N., et
1023 al., 2007. The origin of the 1500-year climate cycles in Holocene North-Atlantic records.
1024 *Climate of the Past* 3, 569-575.
1025

1026 Debret, M., Sebag, D., Crosta, X., Massei, N., Petit, J-R, Chapron, E, et al., 2009. Evidence
1027 from wavelet analysis for a mid-Holocene transition in global climate forcing. *Quaternary*
1028 *Science Reviews* 28, 2675-2688.
1029

1030 De Jong, R., Björck, S., Björkman, L., Clemmensen, L.B., 2006. Storminess variation during
1031 the last 6500 years as reconstructed from an ombrotrophic peat bog in Halland, SW Sweden.
1032 *Journal of Quaternary Science* 21, 905-919.
1033

1034 De Jong, R., Schoning, K., Björck, S., 2007. Increased aeolian activity during humidity shifts
1035 as recorded in a raised bog in south-west Sweden during the peast 1700 years. *Climate of the*
1036 *Past* 3, 411-422.
1037

1038 Delaine, M., Châtelet, E., Bout-Roumazielles, V., Goubert, E., Le Cadre, E., Recourt, P.,
1039 Trentesaux, A., Arthuis, R., 2015. Multiproxy approach for Holocene paleoenvironmental
1040 reconstructions from microorganisms (testate amoebae and foraminifera) and sediment
1041 analyses: The infilling of the Loire Valley in Nantes (France). *The Holocene* 25, 407-420.
1042

1043 de Vernal, A., Hillaire-Marcel, C., 2006. Provincialism in trends and high frequency changes
1044 in the northwest North Atlantic during the Holocene. *Global and Planetary Change* 54, 263-
1045 290.
1046

1047 de Vernal, A., Henry, M., Bilodeau, G., 1999. Technique de préparation et d'analyse en
1048 micropaléontologie. *Les Cahiers du GEOTOP vol. 3*, Université du Québec à Montréal,
1049 Montréal, Canada.
1050

1051 de Vernal, A., Hillaire-Marcel, C., Rochon, A., Fréchette, B., Henry, M., Solignac, S.,
1052 Bonnet, S., 2013. Dinocyst-based reconstructions of sea ice cover concentration during the

1053 Holocene in the Arctic Ocean, the northern North Atlantic Ocean and its adjacent seas.
1054 Quaternary Science Reviews 79, 111-121.
1055
1056 Dubrulle, C., Jouanneau, J.M., Lesueur, P., Bourillet, J.F., Weber, O., 2007. Nature and rates
1057 of fine-sedimentation on a mid-shelf: “La Grande Vasière” (Bay of Biscay, France).
1058 Continental Shelf Research 27, 2099-2115.
1059
1060 Durand, M., Mojtahid, M., Maillet, G.M., Murat, A., Baltzer, A., Schmidt, S., Blet, S.,
1061 Garlan, T., Marchès E., Howa, H. 2018. Late Holocene record from the Loire incised
1062 paleovalley (Bay of Biscay, Northeast Atlantic): insights into regional and global forcing
1063 factors. Palaeogeography, Palaeoclimatology, Palaeoecology 511, 12-28.
1064
1065 Dussud, L., 2010. CABTEX cruise, RV Pourquoi pas ? Sismer: doi:10.17600/10030050.
1066
1067 Dyke, A.S., 2004. An outline of North American deglaciation with emphasis on central and
1068 northern Canada. Quaternary Glaciations: Extent and Chronology 2, 373-424.
1069
1070 Eynaud, F., Mary, Y., Zumaque, J., Wary, M., Gasparotto, M.C., Swingedouw, D., Colin, C.,
1071 2018. Compiling multiproxy quantitative hydrographic data from Holocene marine archives
1072 in the North Atlantic: A way to decipher oceanic and climatic dynamics and natural modes?
1073 Global and Planetary Change 170, 48-61.
1074
1075 Fatela, F., Taborda, R., 2002. Confidence limits of species proportions in microfossil
1076 assemblages, Marine Micropaleontology 45, 169-174.
1077
1078 Fernane, A., Gandouin, E., Penaud, A., Van Vliet-Lanoë, B., Goslin, J., Vidal, M., Delacourt,
1079 C., 2014. Coastal palaeoenvironmental record of the last 7 ka BP in NW France: sub-
1080 millenary climatic and anthropic Holocene signals. The Holocene 24, 1785-1797.
1081
1082 Fernane, A., Penaud, A., Gandouin, E., Goslin, J., Van Vliet-Lanoë, B., Vidal, M., 2015.
1083 Climate variability and storm impacts as major drivers for human coastal marsh withdrawal
1084 over the Neolithic period (Southern Brittany, NW France). Palaeogeography,
1085 Palaeoclimatology, Palaeoecology 435, 136-144.
1086
1087 Ferrer, L., Fontán, A., Mader, J., Chust, G., González, M., Valencia, V., Uriarte, A., Collins,
1088 M. B., 2009. Low-salinity plumes in the oceanic region of the Basque Country. Continental
1089 Shelf Research 29, 970-984.
1090
1091 **Figuerola, R.I., Bravo, I., 2005. Sexual reproduction and two different encystment strategies of**
1092 ***Lingulodinium polyedrum* (Dinophyceae) in culture. Journal of Phycology 41, 370-379.**
1093
1094 Frew, R.D., Dennis, P.F., Heywood, K.J., Meredith, M.P., Boswell, S.M., 2000. The oxygen
1095 isotope composition of water masses in the northern North Atlantic. Deep-Sea Res. I
1096 Oceanogr. Res. Pap. 47, 2265-2286.
1097
1098 Frouin, R., Fiúza, A.F.G., Ambar, I., Boyd, T.J., 1990. Observations of a poleward surface
1099 current off the coasts of Portugal and Spain during winter. Journal of Geophysical Research
1100 95, 679-691.
1101

1102 Ganne A., Leroyer C., Penaud A., Mojtahid M., 2016. Present-day palynomorph deposits in
1103 an estuarine context: the case of the Loire Estuary. *Journal of Sea Research* 118, 35-51.
1104

1105 Garcia, J., Mojtahid, M., Howa, H., Michel, E., Schiebel, R., Charbonnier, C., Anschutz, P.,
1106 Jorissen, F. 2013. Benthic and planktic foraminifera of the last 12.8 cal ka BP in the
1107 southeastern Bay of Biscay: Paleoenvironmental implications. *Acta Protozoologica* 52, 161-
1108 180.
1109

1110 García-Artola, A., Stéphan, P., Cearreta, A., Kopp, R.E., Khan, N.S., Horton, B.P., 2018.
1111 Holocene sea-level database from the Atlantic coast of Europe. *Quaternary Science Reviews*
1112 196, 177-192.
1113

1114 Garcia-Soto, C, Pingree, RD, 2012. Atlantic Multidecadal Oscillation (AMO) and sea surface
1115 temperature in the Bay of Biscay and adjacent regions. *Journal of the Marine Biological*
1116 *Association of the United Kingdom* 92, 213-234.
1117

1118 Gaudin, L., 2004. Transformations spatio-temporelles de la végétation du nordouest de la
1119 France depuis la fin de la dernière glaciation. Reconstitutions paléo-paysagères. Thèse
1120 doctorat, université de Rennes I, 660 pp.
1121

1122 Giraudeau, J., Grelaud, M., Solignac, S., Andrews, J., Moros, M., Jansen, E., 2010.
1123 Millennial-scale variability in Atlantic water advection to the Nordic seas derived from
1124 Holocene coccolith concentration records. *Quaternary Science Reviews* 29, 1276-1287.
1125

1126 Goslin, J., Fruergaard, M., Sander, L., Gałka, M., Menviel, L., Monkenbusch, J., Thibault, N.,
1127 Clemmensen, L.B., 2018. Holocene centennial to millennial shifts in North-Atlantic
1128 storminess and ocean dynamics. *Scientific Reports* 8, 12778.
1129

1130 Goslin, J., Gałka, M., Sander, L., Fruergaard, M., Mokenbusch, J., Thibaut, N., Clemmensen,
1131 L.B., Fruergaard, M., Sander, L., 2019. Decadal variability of north-eastern Atlantic
1132 storminess at the mid-Holocene: New inferences from a record of wind-blown sand, western
1133 Denmark. *Global and Planetary Change* 180, 16-32.
1134

1135 Guillaud, J, Aminot, A, Delmas, D, Gohin, F, Lunven, M, Labry, C, et al., 2008. Seasonal
1136 variation of riverine nutrient inputs in the northern Bay of Biscay (France), and patterns of
1137 marine phytoplankton response. *Journal of Marine Systems* 72, 309-319.
1138

1139 Hammer, Ø., Harper, D.A.T., Ryan, P.D., 2001. Past: Paleontological Statistics Software
1140 Package for Education and Data Analysis. *Palaeontologia Electronica*, vol. 4, issue 1, art. 4:
1141 9pp., 178kb. http://palaeo-electronica.org/2001_1/past/issue1_01.htm.
1142

1143 Harper, D.A.T. (ed.). 1999. *Numerical Palaeobiology*. John Wiley & Sons, Chichester.
1144

1145 Hoogakker, B.A., Chapman, M.R., McCave, I.N., Hillaire-Marcel, C., Ellison, C.R., Hall,
1146 I.R., Telford, R.J., 2011. Dynamics of North Atlantic deep water masses during the Holocene.
1147 *Paleoceanography* 26. <https://doi.org/10.1029/2011PA002155>.
1148

1149 Hurrell, JW, 1995. Decadal trends in the North Atlantic Oscillation: regional temperatures
1150 and precipitation. *Science* 269, 676-679.
1151

1152 Hurrell, JW, Kushnir, Y, Ottersen, G, Visbeck, M, 2003. The North Atlantic Oscillation:
1153 Climatic Significance and Environmental Impact. Geophysical Monograph Series 134, 279
1154 pp.
1155
1156 Isemer, H.-J., Hasse, L., 1985. The Bunker Climate Atlas of the North Atlantic Ocean, 2 Vols.
1157 Springer, Berlin. 218 and 252 pp.
1158
1159 Joly, C., Visset, L., 2009. Evolution of vegetation landscapes since the Late Mesolithic on the
1160 French West Atlantic coast. Review of Palaeobotany and Palynology 154, 124-179.
1161
1162 Jouanneau, JM, Weber, O, Cremer, M, Castaing, P, 1999. Fine-grained sediment budget on
1163 the continental margin of the Bay of Biscay. Deep Sea Research Part II: Topical Studies in
1164 Oceanography 46, 2205-2220.
1165
1166 Kaplan, M.R., Wolfe, A.P., 2006. Spatial and temporal variability of Holocene temperature in
1167 the North Atlantic region. Quaternary Research 65, 223-231.
1168
1169 Kissel, C., Toer, A.V., Laj, C., Cortijo, E., Michel, E., 2013. Variations in the strength of the
1170 North Atlantic bottom water during Holocene. Earth Planetary Science Letters 369-370, 248-
1171 259.
1172
1173 Koutsikopoulos, C., Le Cann, B., 1996. Physical processes and hydrological structures related
1174 to the Bay of Biscay anchovy. Sci. Mar. 60, 9-19.
1175
1176 Lambert C., Vidal M., Penaud A., Combourieu-Nebout N., Lebreton V., Ragueneau O.,
1177 Gregoire G., 2017. Modern palynological record in the Bay of Brest (NW France): Signal
1178 calibration for palaeo-reconstructions. Review of Palaeobotany and Palynology 244, 13-25.
1179
1180 Lambert, C., Penaud, A., Vidal, M., Klouch, K., Gregoire, G., Ehrhold, A., Eynaud, F.,
1181 Schmidt, S., Ragueneau, O., Siano, R., 2018. Human-induced river runoff overlapping natural
1182 climate variability over the last 150 years: Palynological evidence (Bay of Brest, NW France).
1183 Global and Planetary Change 160, 109-122.
1184
1185 Lambert C., Vidal M., Penaud A., Le Roy P., Goubert E., Paillet Y., Stéphan P., Ehrhold A.,
1186 2019. Palaeoenvironmental reconstructions during the Meso- to Neolithic transition (9.2 – 5.3
1187 cal ka BP) in Northwestern France: palynological evidences. The Holocene 29, 380-402.
1188
1189 Lambert, C., Penaud, A., Vidal, M., Erhold, A., [pers. com.](#) North Atlantic oceanic and
1190 atmospheric configurations as Western Europe main environment and climate changes drivers
1191 over the late Holocene.
1192
1193 Lazure, P, Jégou, AM, 1998. 3D modelling of seasonal evolution of Loire and Gironde
1194 plumes on Biscay Bay continental shelf. Oceanologica Acta 21, 165-177.
1195
1196 Lazure, P., Dumas, F., Vrignaud, C., 2008. Circulation on the Armorican shelf (Bay of
1197 Biscay) in autumn. J. Mar. Syst. 72, 218-237.
1198
1199 Le Boyer, A., Charria, G., Le Cann, B., Lazure, P., Marié, L., 2013. Circulation on the shelf
1200 and the upper slope of the Bay of Biscay. Continental Shelf Research 55, 97-107.
1201

1202 Le Cann, B., Serpette, A., 2009. Intense warm and saline upper ocean inflow in the southern
1203 Bay of Biscay in autumn-winter 2006-2007. *Continental Shelf Research* 29, 1014–1025.

1204 Lesueur, P., Jouanneau, J.M., Boust, D., Tastet, J.P., Weber, O., 2001. Sedimentation rates
1205 and fluxes in the continental shelf mud fields in the Bay of Biscay (France). *Continental Shelf*
1206 *Research* 21, 1383-1401.

1207

1208 Lohmann, K., Drange, H., Bentsen, M., 2009. Response of the North Atlantic subpolar gyre to
1209 persistent North Atlantic oscillation like forcing. *Climate Dynamics* 32, 273-285.

1210

1211 Mangerud, J, Bondevik, S, Gulliksen, S, Karin Hufthammer, A, Høisæter, T, 2006. Marine
1212 ¹⁴C reservoir ages for 19th century whales and molluscs from the North Atlantic. *Quaternary*
1213 *Science Reviews* 25, 3228-3245.

1214

1215 Marcott, S.A., Shakun, J.D., Clark, P.U., Mix, A.C., 2013. A reconstruction of regional and
1216 global temperature for the past 11,300 years. *Science* 339, 1198-1201.

1217

1218 Marret, F., Zonneveld, K.A.F., 2003. Atlas of modern organic-walled dinoflagellate cyst
1219 distribution. *Review of Palaeobotany and Palynology* 125, 1-200.

1220

1221 **Marret, F., Scourse, J., Austin, W., 2004. Holocene shelf-sea seasonal stratification dynamics:**
1222 **A dinoflagellate cyst record from the Celtic Sea, NW European shelf. *The Holocene* 14, 689-**
1223 **696.**

1224

1225 Mary, Y, Eynaud, F, Colin, C, Rossignol, L, Brocheray, S, Mojtahid, M, et al., 2017. Changes
1226 in Holocene meridional circulation and poleward Atlantic flow: the Bay of Biscay as a nodal
1227 point. *Clim. Past* 13, 201-216.

1228

1229 Mayewski, P.A., Rohling, E.E., Curt Stager, J., Karlén, W., Maasch, K.A., David Meeker, L.,
1230 Meyerson, E.A., Gasse, F., Vvan Kreveld, S., Holmgren, K., Lee-Thorp, J., Rosqvist, G.,
1231 Rack, F., Staubwasse, M., Schneider, R.R., Steig, E.J., 2004. Holocene climate variability.
1232 *Quaternary Research* 62, 243-255.

1233

1234 Menier, D., Tessier, B., Proust, J.-N., Baltzer, A., Sorrel, P., Traini, C., 2010. The Holocene
1235 transgression as recorded by incised-valley infilling in a rocky coast context with low
1236 sediment supply (southern Brittany, western France). *Bulletin de la Société Géologique de*
1237 *France* 181, 115-128.

1238

1239 Mertens, K.N., Verhoeven, K., Verleye, T., Louwye, S., Amorim, A., Ribeiro, S., ...
1240 González, C., 2009. Determining the absolute abundance of dinoflagellate cysts in recent
1241 marine sediments: the *Lycopodium* marker-grain method put to the test. *Rev. Palaeobot.*
1242 *Palynol.* 157, 238-252.

1243

1244 Mojtahid, M., Jorissen, F.J., Garcia, J., Schiebel, R., Michel, E., Eynaud, F., et al., 2013. High
1245 resolution Holocene record in the southeastern Bay of Biscay: Global versus regional climate
1246 signals. *Palaeogeography, Palaeoclimatology, Palaeoecology* 377, 28-44.

1247

1248 Mojtahid M., Durand M., Coste P-O., Toucanne S., Howa H., Nizou J., Eynaud F., Penaud
1249 A., 2019. Millennial-scale Holocene hydrological changes in the northeast Atlantic: New
1250 insights from ‘La Grande Vasière’ mid-shelf mud belt. *The Holocene* 29, 467-480.

1251

- 1252 Morley, A., Rosenthal, Y., Demenocal, P., 2014. Ocean-atmosphere climate shift during the
1253 mid-to-late Holocene transition. *Earth Planet. Sci. Lett.* 388, 18-26.
- 1254
- 1255 Morzadec-Kerfourn, M.-T., 1974. Variations de la ligne de rivage armoricaine au Quaternaire.
1256 Analyses polliniques de dépôts organiques littoraux. *Mémoires de la Société Géologique et*
1257 *Minéralogique de Bretagne* 17, 208 pp.
- 1258
- 1259 Morzadec-Kerfourn, M.-T., 1976. La signification écologique des dinoflagellés et leur intérêt
1260 pour l'étude des variations du niveau marin. *Revue de Micropaléontologie* 18, 229-235.
- 1261
- 1262 Morzadec-Kerfourn, M.-T., 1977. Les kystes de Dinoflagellés dans les sédiments récents le
1263 long des côtes bretonnes. *Revue de Micropaléontologie* 20, 157-166.
- 1264
- 1265 Morzadec-Kerfourn, M.-T., 1992. Upper Pleistocene and Holocene dinoflagellate cyst
1266 assemblages in marine environments of the Mediterranean Sea and the north-west Atlantic
1267 coast of France. In: Head, M.J., and Wrenn, J.H. (eds.), *Neogene and Quaternary*
1268 *Dinoflagellate Cysts and Acritarchs: American Association of Stratigraphic Palynologists*
1269 *Foundation, Dallas*, 121-132.
- 1270
- 1271 Morzadec-Kerfourn, M.-T., 1995. Coastline Changes in the Armorican Massif (France)
1272 During the Holocene. *Journal of Coastal Research Special Issue* 17, 197-203
- 1273
- 1274 Morzadec-Kerfourn, M.-T., 1997. Dinoflagellate cysts and the paleoenvironment of Late-
1275 Pliocene early-pleistocene deposits of Brittany, Northwest France. *Quaternary Science*
1276 *Reviews* 16, 883-898.
- 1277
- 1278 Naughton, F., Bourillet, J.-F., Sanchez Goni, M.F., Turon, J.-L., Jouanneau, J.-M., 2007.
1279 Long-term and millennial-scale climate variability in northwestern France during the last
1280 8850 years. *The Holocene* 17, 939-953.
- 1281
- 1282 Olsen, J., Anderson, N.J., Knudsen, M.F., 2012. Variability of the Atlantic Oscillation over
1283 the past 5,200 years. *Nature Geoscience* 5, 808-812.
- 1284
- 1285 Orme, L.C., Miettinen, A., Divine, D., Husum, K., Pearce, C., Van Nieuwenhove, N., Born,
1286 A., Mohan, R., Seidenkrantz, M.S., 2018. Subpolar North Atlantic sea surface temperature
1287 since 6 ka BP: Indications of anomalous ocean-atmosphere interactions at 4-2 ka BP.
1288 *Quaternary Science Reviews* 194, 128-142.
- 1289
- 1290 Ouguerram, A., Visset, L., 2001. Histoire de la végétation et première mise en évidence d'un
1291 milieu marin pendant l'Holocène dans la vallée de l'Erdre et le val de Gesvres (bassin versant
1292 de la Loire, Massif armoricain, France). *Quaternaire* 12, 189-199.
- 1293
- 1294 Pailler, Y., Nicolas, C., 2019. Une maison sous les dunes : Beg Ar Loued, île Molène,
1295 Finistère. Identité et adaptation des groupes humains en Mer d'Iroise à la transition IIIe-Ile
1296 millénaire avant notre ère. Edition Sidestone Press, Leiden. ISBN: 978-9-088-90380-9. 736
1297 pp.
- 1298
- 1299 Penaud, A., Eynaud, F., Turon, J.L., Zaragosi, S., Marret, F., Bourillet, J.F., 2008. Interglacial
1300 variability (MIS 5 and MIS 7) and dinoflagellate cyst assemblages in the Bay of Biscay
1301 (North Atlantic). *Marine Micropaleontology* 68, 136-155.

1302
1303 Pingree, RD, Le Cann, B, 1989. Celtic and Armorican slope and shelf residual currents.
1304 Progress in Oceanography 23, 303-338.
1305
1306 Pingree, RD, Le Cann, B, 1992a. Three anticyclonic Slope Water Oceanic eDDIES
1307 (SWODDIES) in the southern Bay of Biscay in 1990. Deep Sea Research Part A.
1308 Oceanographic Research Papers 39, 1147-1175.
1309
1310 Pingree, RD, Le Cann, B, 1992b. Anticyclonic eddy X91 in the southern Bay of Biscay, May
1311 1991 to February 1992. Journal of Geophysical Research 97, 14353-14.
1312
1313 Pouzet, P., Maanan, M., Piotrowska, N., Baltzer, A., Stéphan, P., Robin, M., 2018.
1314 Chronology of Holocene storm events along the European Atlantic coast: New data from the
1315 Island of Yeu, France. Progress in Physical Geography 42, DOI:
1316 10.1177/0309133318776500.
1317
1318 Puillat, I, Lazure, P, Jégou, AM, Lampert, L, Miller, PI, 2004. Hydrographical variability on
1319 the French continental shelf in the Bay of Biscay, during the 1990s. Continental Shelf
1320 Research 24, 1143-1163.
1321
1322 Reid, P.C., 1974. Gonyaulacacean dinoflagellate cysts from the British Isles. Nova Hedwigia
1323 25, 579-637.
1324
1325 Reid, P.C., 1975. A regional sub-division of dinoflagellate cysts around the British Isles. The
1326 New Phytologist 75, 589-603.
1327
1328 Reimer, P.J., Bard, E., Bayliss, A., Beck, J.W., Blackwell, P.G., Ramsey, C.B., et al., 2013.
1329 IntCal13 and Marine13 Radiocarbon Age Calibration Curves 0–50,000 Years cal BP.
1330 Radiocarbon 55, 1869-1887.
1331
1332 Renssen, H., Seppä, H., Crosta, X., Gosse, H., Roche, D.M., 2012. Global characterization
1333 of the Holocene Thermal Maximum. Quaternary Science Reviews 48, 7-19.
1334
1335 Rochon, A., Vernal, A.d., Turon, J.-L., Matthießen, J., Head, M., 1999. Distribution of recent
1336 dinoflagellate cysts in surface sediments from the North Atlantic Ocean and adjacent seas in
1337 relation to sea-surface parameters. American Association of Stratigraphic Palynologists
1338 Contribution Series. 35, 1-146.
1339
1340 Rossignol, M., 1964. Hystrichosphères du Quaternaire en Méditerranée orientale dans les
1341 sédiments pléistocènes et les boues marines actuelles. Revue de Micropaléontologie 7, 83-99.
1342
1343 Rossignol, M., Gayet, M., Dubertret, L., André, C., Delienne, L., 1969. Sédimentation
1344 palynologique dans le domaine marin quaternaire de Palestine. Notes et Mémoires Moyen-
1345 Orient 10, 272 pp.
1346
1347 Ruddiman, W.F., Fuller, D.Q., Kutzbach, J.E., Tzedakis, P.C., Kaplan, J.O., Ellis, E.C.,
1348 Vavrus, S.J., Roberts, C.N., Fyfe, R., He, F., Lemmen, C., Woodbridge, J., 2016. Late
1349 Holocene climate: natural or anthropogenic? Rev. Geophys. 54, 93-118.
1350

1351 Solabarrieta, L., Rubio, A., Castanedo, S., Medina, R., Charria, G., Hernandez, C., 2014.
1352 Surface water circulation patterns in the southeastern Bay of Biscay: New evidences from HF
1353 radar data. *Continental Shelf Research* 74, 60-76.
1354
1355 Solignac, S., Giraudeau, J., de Vernal, A., 2006. Holocene sea surface conditions in
1356 the western North Atlantic: spatial and temporal heterogeneities. *Paleoceanography* 21,
1357 10.1029/2005PA001175.
1358
1359 Solignac, S., Grelaud, M., de Vernal, A., Giraudeau, J., Moros, M., McCave, I.N., Hoogakker,
1360 B., 2008. Reorganization of the upper ocean circulation in the mid-Holocene in the
1361 northeastern Atlantic. *Can. J. Earth Sci.* 45, 1417-1433.
1362
1363 Sorrel, P., Debret, M., Billeaud, I., Jaccard, S.L., McManus, J.F., Tessier, B., 2012. Persistent
1364 non-solar forcing of Holocene storm dynamics in coastal sedimentary archives. *Nature*
1365 *Geoscience* 5, 892-896.
1366
1367 Steinhilber, F., Beer, J., Zröhlich, C., 2009. Total solar irradiance during the Holocene.
1368 *Geophysical Research Letters* 36, L19704.
1369
1370 Stéphan, P., Pailler, Y., Tresset, A., Gandois, H., 2013. Changements paléogéographiques de
1371 l'archipel de Molène (Finistère, Bretagne, France): implications sur les peuplements humains
1372 du Néolithique à l'Age du Bronze. In Daire, M.Y., Dupont, C., Baudry, A., Billard, C., Large,
1373 J.M., Lespez, L., Normand, E., Scarre, C., (Eds.). *Ancient Maritime Communities and the*
1374 *Relationship between People and Environment along the European Atlantic Coasts.*
1375 *Proceedings of the HOMER 2011 Conference, Vannes (France), British Archaeological*
1376 *Reports, International Series 2570, Oxford: Archaeopress, 647-660.*
1377
1378 Stéphan, P., Goslin, J., Pailler, Y., Manceau, R., Suanez, S., Van Vliet-Lanoë, B., Hénaff, A.,
1379 Delacourt, C., 2015. Holocene salt-marsh sedimentary infillings and relative sea-level
1380 changes in West Brittany (France) from foraminifera-based transfer functions. *Boreas* 44,
1381 153-177.
1382
1383 Stéphan, P., Marguerie, D., Aoustin, D., Fichaut, B., Suanez, S., 2018. Changements
1384 paléogéographiques dans l'archipel de Molène, du Néolithique à aujourd'hui. In Y. Pailler
1385 and C. Nicolas (dir.). *Une maison sous les dunes : Beg Ar Loued, île Molène, Finistère.*
1386 *Identité et adaptation des groupes humains en Mer d'Iroise à la transition IIIe-IIe millénaire*
1387 *avant notre ère. Edition Sidestone Press, Leiden., pp.69-107. ISBN: 978-9-088-90380-9.*
1388
1389 Stéphan, P., Verdin, F., Arnaud-Fassetta, G., Bertrand, F., Eynaud, F., García-Artola, A.,
1390 Bosq, M., Culioli, C., Suanez, S., Coutelier, C., Bertran, P., Colin, A., Costa, S., 2019.
1391 Holocene coastal changes along the Gironde estuary (SW France): new insights from the
1392 North Medoc peninsula beach/dune system. *Quaternaire* 30, 47-75.
1393
1394 Stockmarr, J., 1971. Tablets with spores used in absolute pollen analysis. *Pollen et Spores* 13,
1395 615-621.
1396
1397 Stuiver, M., Reimer, P.J., 1993. Extended 14C database and revised CALIB radiocarbon
1398 calibration program. *Radiocarbon* 35, 215-230.
1399

1400 Sutton, R., Allen, M., 1997. Decadal predictability of North Atlantic sea surface temperature
1401 and climate. *Nature* 388, 563-567.
1402

1403 Tenailon, M.I., Charcosset, A. 2011. A European perspective on maize history. *C. R. Biol.*
1404 334, 221-228.
1405

1406 Ters, M, Planchais, N, Azema, C, 1968. L'évolution de la basse vallée de la Loire, à l'aval de
1407 Nantes, à la fin du Würm et pendant la transgression flandrienne. *Bulletin de l'Association*
1408 *française pour l'étude du quaternaire* 5, 217-246
1409

1410 Thornalley, D.J.R., Elderfield, H., McCave, I.N., 2009. Holocene oscillations in temperature
1411 and salinity of the surface subpolar North Atlantic. *Nature* 457, 711-714.
1412

1413 Tisdall, E.W., McCulloch, R.D., Sanderson, D.C.W., Simpson, I.A., Woodward, N.L., 2013.
1414 Living with sand: A record of landscape change and storminess during the Bronze and Iron
1415 Ages Orkney, Scotland. *Quaternary International* 308-309, 205-215.
1416

1417 Tréguer, P, Goberville, E, Barrier, N, L'Helguen, S, Morin, P, Bozec, Y, et al., 2014. Large
1418 and local-scale influences on physical and chemical characteristics of coastal waters of
1419 Western Europe during winter. *Journal of Marine Systems* 139, 79-90.
1420

1421 Turon, J. L., 1984. Le palynoplancton dans l'environnement actuel de l'Atlantique Nord-
1422 oriental. Evolution climatique et hydrologique depuis le dernier maximum glaciaire.
1423 *Mémoires de l'Institut de Géologie du Bassin d'Aquitaine* 17, 313 pp.
1424

1425 van Vliet-Lanoe, B., Penaud, A., Henaff, A., Delacourt, C., Fernane, A., Goslin, J.,
1426 Hallegouet, B., Le Cornec, E., 2014. Middle- to late-Holocene storminess in Brittany (NW
1427 France): part II - the chronology of events and climate forcing. *The Holocene* 24, 434-453.
1428

1429 Van Vliet-Lanoe, B., Goslin, J. , Hénaff, A., Hallégouët, B., Delacourt, C., Le Cornec, E. ,
1430 Meurisse-Fort, M.. 2016. The Holocene formation and evolution of coastal dune ridges,
1431 Brittany (France).*CR Géosciences* 348, 462-470.
1432

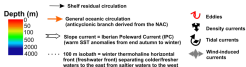
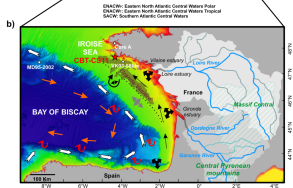
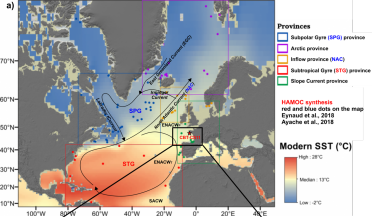
1433 Vincent, A, Kurc, G, 1969. Hydrologie. Variations saisonnières de la situation thermique du
1434 golfe de gascogne en 1967. *Revue travaux Institut pêches maritimes* 33, 79-96.
1435

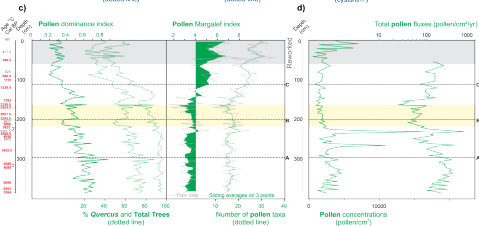
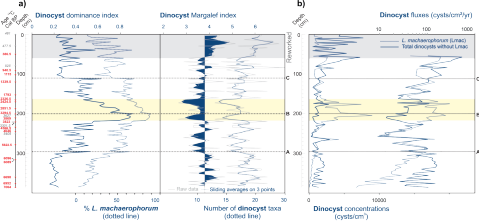
1436 Vinther, B.M., Clausen, H.B., Johnsen, S.J., Rasmussen, S.O., Andersen, K.K., Buchardt,
1437 S.L., Dahl-Jensen, D., Seierstad, I.K., Siggaard-Andersen, M.-L., Steffensen, J. P., Svensson,
1438 A., Olsen, J., Heinemeier, J., 2006. A synchronized dating of three Greenland ice cores
1439 throughout the Holocene. *Journal of Geophysical Research* 111,
1440 <https://doi.org/10.1029/2005JD006921>.
1441

1442 Voelker, A.H.L., Colman, A., Olack, G., Waniek, J.J., Hodell, D., 2015. Oxygen and
1443 hydrogen isotope signatures of Northeast Atlantic water masses. *Deep Sea Research Part II:*
1444 *Topical Studies in Oceanography* 116, 89-106.
1445

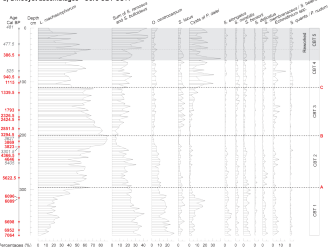
1446 Wall, D., Dale, B., Lohmann, G.P., Smith, W.K., 1977. The environment and climatic
1447 distribution of dinoflagellate cysts in modern marine sediments from regions in the north and
1448 south Atlantic oceans and adjacent seas. *Marine Micropaleontology* 2, 121-200.
1449

- 1450 Wanner, H., Beer, J., Bütikofer, J., Crowley, T.J., Cubasch, U., Flückiger, J., et al., 2008.
1451 Mid- to Late Holocene climate change: an overview. *Quaternary Science Reviews* 27, 1791-
1452 1828.
- 1453
1454 Williams, D.B., 1971. The occurrence of Dinoflagellates in marine sediments. *In the*
1455 *Micropaleontology of Ocean*, Funnel B.M. and Riedel W.R. Edit., 231-243.
- 1456
1457 Yelekçi, O., Charria, G., Capet, X., Reverdin, G., Sudre, J., Yahia, H., 2017. Spatial and
1458 seasonal distributions of frontal activity over the French continental shelf in the Bay of
1459 Biscay. *Continental Shelf Research* 144, 65-79.
- 1460
1461 Zaragosi, S., Eynaud, F., Pujol, C., Auffret, G., Turon, J.-L., Garlan, T., 2001. Initiation of the
1462 European deglaciation as recorded in the northwestern Bay of Biscay slope environments
1463 (Meriadzek Terrace and Trevelyan Escarpment): a multi-proxy approach. *Earth Planetary*
1464 *Science Letters* 188, 493-507.
- 1465
1466 Zonneveld, K.A.F., Marret, F., Versteegh, G.J.M., Bogus, K., Bonnet, S., Bouimtarhan, I., et
1467 al., 2013. Atlas of modern dinoflagellate cyst distribution based on 2405 data points. *Review*
1468 *of Palaeobotany and Palynology* 191, 1-197.
- 1469
1470 Zumaque, J., Eynaud, F., de Vernal, A., 2017. Holocene paleoceanography of the Bay of
1471 Biscay: evidence for west-east linkages in the North Atlantic based on dinocyst data.
1472 *Palaeogeogr. Palaeoclimatol. Palaeoecol.* 468, 403-413.





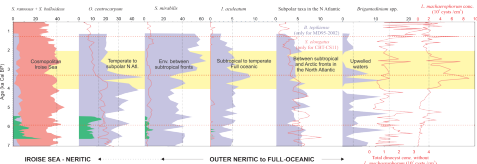
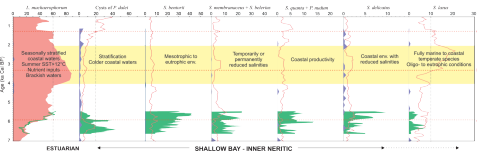
a) Dinocyst assemblages - Core CBT-CS11



b) Pollen assemblages - Core CBT-CS11



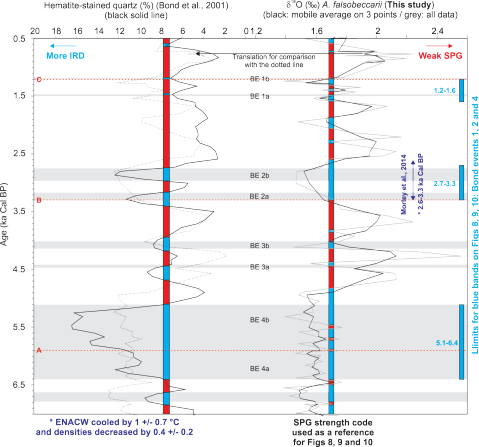
Percentages of dinocyst taxa on a proximal-distal gradient : percentages of taxa represented without *L. machaerophorum* counts in the main sum for A and CBT-CS11 cores

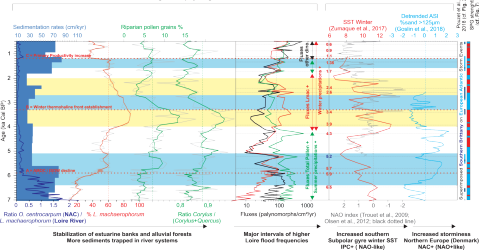


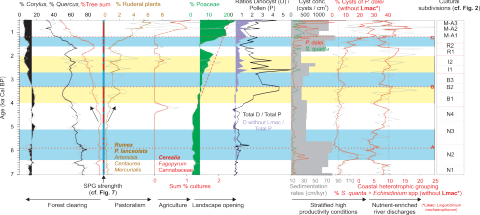
Slope, MD95-2002
 2174m water depth

Shelf, CBT-CS11
 73m water depth

Bay of Brest, Core A
 8.2 m water depth



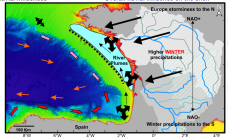
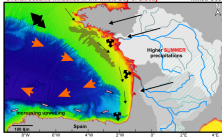




A) = Summer prevailing mode = (until 5.9 ka BP)
Overall oceanic influence in the whole Bay of Biscay

• Autumn mode = (especially 5.9 to 4 ka BP)
Mixed Oceanic-Fluvial Influences

B) = Winter prevailing mode = (from 3.3 ka BP)
Overall fluvial influence on the shelf



Orbitally-driven hydrographic changes

A)

- Shelf residual circulation : stronger **summer NW-SE** direction and weaker **winter SE-NW** direction
- Slope current : **less intense IPC** influence to the southern and northern Bay of Biscay

B)

- Shelf residual circulation : stronger **winter SE-NW** direction and weaker **summer SW-SE** direction
- Slope current : **more intense IPC** influence to the southern and northern Bay of Biscay

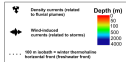
Oceanic-driven millennial climate changes (superimposed on A) or B) : example with strong SPO on A) (and weak SPO on B) above)



Strengthened Subpolar Gyre :
 Increased BMACW = Polar = signature in the Boll
 Intensified northward heat transport through the NAO
 until the Nordic seas
 Increased SST South of Iceland (Iringer Current)
 Northern European storminess (Goslin et al., 2018)
NAO+ prevailing configuration



Weakened Subpolar Gyre :
 Increased BMACW = Tropical = signature in the Boll
 Decreased North Atlantic oceanic influence through
 the NAO recirculation in the Boll
 Increased winter SST in the NE Atlantic Ocean : stronger IPC (MDS-2002)
 Decreased SST South of Iceland (Dima et al., 2016 - etc 4-2 ka interval)
NAO- prevailing configuration



Code	Depth (cm)	Sample nature	Age 14C BP	Error	Age min (mean) max Cal BP
<i>SacA41576</i>	0*	<i>Turritella communis</i>	720	30	457(481)505
<i>SacA 32019</i>	29*	Bivalve	715	35	451(477.5)504
<i>SacA 32020</i>	50	<i>Turritella communis</i>	645	30	305(386.5)468
<i>Poz-71200</i>	79*	<i>Turritella communis</i>	820	30	501(525)549
<i>SacA 32021</i>	91	<i>Turritella communis</i>	1340	30	923(940.5)958
<i>SacA38446</i>	101	Bivalve	1505	30	1049(1115)1181
<i>SacA39684</i>	120	<i>Turritella communis</i>	1765	30	1297(1339.5)1382
<i>SacA39683</i>	151	<i>Turritella communis</i>	2180	35	1713(1793)1873
<i>SacA 32022</i>	165	<i>Turritella communis</i>	2600	30	2307(2326.5)2346
<i>SacA38447</i>	170	<i>Turritella communis</i>	2750	30	2360(2424.5)2489
<i>SacA 32023</i>	187	<i>Turritella communis</i>	3080	30	2777(2851.5)2926
SacA55615	200	Bivalve	3410	30	3219(3294.5)3370
<i>SacA 32024</i>	203*	<i>Dentalium</i>	3695	30	3560(3627)3694
SacA55616	210	<i>Turritella communis</i>	3895	30	3834(3869)3904
<i>Poz-71201</i>	220	<i>Turritella communis</i>	3875	35	3720(3823)3926
<i>SacA39682</i>	220*	<i>Turritella communis</i>	3425	35	3218(3301.5)3385
SacA55617	234	Bivalve	4265	30	4288(4366.5)4445
SacA55618	244	Bivalve	4450	30	4565(4646)4727
<i>SacA39681</i>	250*	<i>Turritella communis</i>	4940	35	5345(5405)5465
<i>SacA39680</i>	278	<i>Turritella communis</i>	5205	35	5583(5622.5)5662
<i>SacA 32025</i>	315	<i>Turritella communis</i>	5650	30	5997(6096)6195
<i>SacA38448</i>	316	<i>Turritella communis</i>	5630	30	5995(6089)6183
<i>SacA 32026</i>	360	Bivalve	6200	30	6667(6698)6729
<i>SacA 32027</i>	376	<i>Turritella communis</i>	6415	30	6910(6952)6994
<i>SacA38449</i>	385	<i>Turritella communis</i>	6480	30	6967(7064)7161

Table 1

CBT-CS11 data	Figures with data (D for Dinocyst and P for Pollen)	Methodology and/or Interpretation of the signal
Radiocarbon dates	Table 1, Figure 1a	Calibration with the Calib 7.1 software using the calibration curve IntCal13 (Stuiver and Reimer, 1993; Reimer et al., 2013), with a reservoir age of -324 years (Mangerud et al., 2006)
Age model	Figure 2b	Bchron package under the R program version 3.5.1
Palynomorph concentrations Pollen (P) – Dinocysts (D)	Figures 3b (D), 3d (P), 5 (D)	Marker grain method with <i>Lycopodium</i> spores (de Vernal et al., 1999; Mertens et al., 2009): calibrated tablets of known numbers of <i>Lycopodium</i> spores are added to each sample before chemical treatments (Stockmarr, 1971)
Palynomorph fluxes	Figures 3b (D), 3d (P), 9 (P and D)	Multiplication of concentrations (taxa/cm ³) by sedimentation rates (cm/kyr), fluxes expressed in taxa/cm ² /kyr
Dominance index	Figures 3a (D), 3c (P)	Dominance ranges from 0 (all taxa are equally present) to 1 (one taxon dominates the community completely)
Diversity (Margalef) index	Figures 3a (D), 3c (P)	Number of taxa per sample (S) and Margalef's richness index: $(S - 1) / \ln(n)$, where n is the number of individuals counted in each sample
Major pollen taxa in assemblages	Figure 4b	Pollen percentages are calculated using a main sum excluding <i>Pinus</i> , spores, and indeterminate pollen grains
Major dinocyst taxa in assemblages	Figures 4a (in depth), 5 (in age)	Dinocyst assemblages are described by the percentages of each species calculated on the basis of the total dinocyst sum including unidentified taxa and excluding pre-Quaternary specimens.
Sum <i>O. centrocarpum</i> and <i>S. elongatus</i>	Figure 8	Grouping of "North Atlantic subpolar gyre influence" taxa according to Detrended Correspondence Analysis analysis performed on dinocyst communities and other environmental variables (Data in Brief). Percentages calculated without Lmac in the main cyst sum.
Ratio <i>O. centrocarpum</i> over <i>L. machaerophorum</i>	Figure 9	Ratio between North Atlantic Current (NAC) tracer and estuarine (Loire) tracer so as to discuss oceanic versus continental influences at the mid-shelf core location
Ratio <i>Corylus</i> over <i>Quercus</i>	Figure 9	As trees in general suffer deforestation in parallel with the increase in Poaceae, the ratio <i>Corylus</i> over <i>Quercus</i> makes it possible to highlight the more pronounced/rapid decline of the corylaie
Ratio Dinocyst / Pollen	Figure 10	Marine versus strict continental tracer allowing to address the influence of both compartments (aquatic and terrestrial realms) in the fine sediment deposits of the mid-shelf
Sum <i>S. quanta</i> and <i>Echinidinium</i> spp.	Figure 10	Grouping of "Coastal heterotrophic" taxa according to Detrended Correspondence Analysis analysis performed on dinocyst communities and other environmental variables (Data in Brief). Percentages calculated without Lmac in the main cyst sum.

$\delta^{13}\text{C}$ and $\delta^{18}\text{O}$ (‰VPDB) <i>A. falsobeccarii</i>	Figures 6, 7	Foraminifera cleaned in a methanol ultrasonic bath for a few seconds, then roasted under vacuum at 380°C for 45 min to remove organic matter. Measurements at the IRMS platform: MAT253 mass spectrometer coupled with a KIEL IV preparation line for benthic species (PSO, Plouzané)
$\delta^{13}\text{C}$ and $\delta^{18}\text{O}$ (‰VPDB) <i>C. refulgens</i>	Figure 6	Mojtahid et al., 2019. Measurements on the GasBenchII platform (PSO, Plouzané)
D50 CaCO₃-free grain-size	Figure 8	Mojtahid et al., 2019. Sediment decarbonation with 1 M hydrochloric acid. Laser diffraction particle size analyzer (Malvern™ Mastersizer 3000; LPG-BIAF, Angers)
XRF data : Log (Zr/Al)	Figure 8	Proxy for coarser sediments quartz-sand according to Canonical Correspondence Analysis conducted on XRF data

Table 2